

Serotonin suppresses slow oscillations by activating somatostatin interneurons via the 5-HT_{2A} receptor

Roberto De Filippo¹, Benjamin R. Rost², Alexander Stumpf¹, Claire Cooper¹, John J. Tukker^{1,2}, Christoph Harms³⁻⁵, Prateep Beed¹, Dietmar Schmitz^{1,2,5*}

¹ Charité – Universitätsmedizin Berlin, Neuroscience Research Center, 10117 Berlin, Germany

² German Centre for Neurodegenerative Diseases (DZNE), 10117 Berlin, German

³ Charité – Universitätsmedizin Berlin and Berlin Institute of Health, Department of Experimental Neurology, 10117 Berlin, Germany.

⁴ Charité – Universitätsmedizin Berlin, Center for Stroke Research Berlin, 10117 Berlin, Germany

⁵ Charité – Universitätsmedizin Berlin, Einstein Center for Neurosciences Berlin, 10117 Berlin, Germany

* Correspondence to: dietmar.schmitz@charite.de

Keywords: serotonin, 5-HT_{2A}, somatostatin interneurons, slow oscillations, MDMA, entorhinal cortex

1 Abstract

2 Serotonin (5-HT) affects multiple physiological processes in the brain and is involved in a
3 number of psychiatric disorders. 5-HT axons reach all cortical areas; however, the precise
4 mechanism by which 5-HT modulates cortical network activity is not yet fully understood. We
5 investigated the effects of 5-HT on slow oscillations (SO), a synchronized cortical network
6 activity universally present across species. SO are observed during slow-wave sleep and
7 anesthesia and are considered the default cortical activity pattern. Combining opto- and
8 pharmacogenetic manipulations with electrophysiological recordings, we discovered that 5-
9 HT inhibits SO within the entorhinal cortex (EC) by activating somatostatin-expressing (Som)
10 interneurons via the 5-HT_{2A} receptor (5-HT_{2AR}). This receptor is involved in the etiology of
11 different psychiatric disorders and mediates the psychological effects of many psychoactive
12 serotonergic drugs, suggesting that 5-HT targeting of Som interneurons may play an
13 important role in these processes.

14 Introduction

15 5-HT is one of the most important neuromodulators in the central nervous system. Projections
16 originating from the Raphe nuclei, the brain-stem structure that comprises the majority of 5-
17 HT releasing neurons in the brain, reach all cortical and sub-cortical area (Descarries et al.,
18 2010). Consequentially, it is not surprising that 5-HT is involved in the regulation of a myriad
19 of physiological functions (e.g. circadian rhythm, mood, memory formation, reward encoding,
20 sexual behavior) and psychiatric disorders including depression, autism, schizophrenia, and
21 anxiety disorders (Monti, 2011, Underwood et al., 2018, Hayes and Greenshaw, 2011, Teixeira et al.,
22 2018, Uphouse and Guptarak, 2010, Nakai et al., 2017).

23 5-HT levels in the brain are closely linked to the sleep-wake cycle. Activity of serotonergic
24 raphe neurons is increased during wakefulness, decreased during slow-wave sleep and
25 virtually silent during REM sleep (McGinty and Harper, 1976, Oikonomou et al., 2019). Cortical
26 activity is also influenced by the behavioral state of the animal: slow-wave sleep (SWS) is
27 generally associated to “synchronized” patterns of activity, characterized by low-frequency
28 global fluctuations, whereas active wakefulness and REM sleep features “desynchronized”
29 network activity in which low-frequency fluctuations are absent. The shifting of cortical
30 networks between different patterns of activity is controlled, at least in part, by
31 neuromodulators (Lee and Dan, 2012). For instance, Acetylcholine (Ach) can profoundly alter
32 cortical network activity by inducing desynchronization via activation of Som interneurons
33 (Chen et al., 2015). However, it is not solely responsible for cortical desynchronization as lesions
34 of cholinergic neurons are not sufficient to abolish desynchronization (Kaur et al., 2008). On the
35 other hand, blocking Ach and 5-HT transmission at the same time causes a complete
36 suppression of cortical desynchronization, even during active behavior, thus suggesting that
37 5-HT plays an important role in desynchronization (Vanderwolf and Baker, 1986). In agreement
38 with this line of thought, electrical and optogenetic stimulation of the Raphe nuclei reduce low
39 frequency (1-10 Hz) power in the cortex thus promoting desynchronization (Puig et al., 2010,
40 Grandjean et al., 2019). Moreover, optogenetic stimulation of serotonergic neurons at a
41 physiological frequency (25 Hz) is sufficient to wake up mice from SWS (Oikonomou et al.,
42 2019). These data suggest a causal relationship between 5-HT levels and cortical activity (Lee
43 and Dan, 2012, Harris and Thiele, 2011). The exact mechanism by which 5-HT modulates network
44 activity in the cortex is, however, still not fully understood.

45 Here, we used electrophysiological techniques together with pharmacology, optogenetics
46 and pharmacogenetics to investigate the effect of 5-HT on SO, a network oscillation

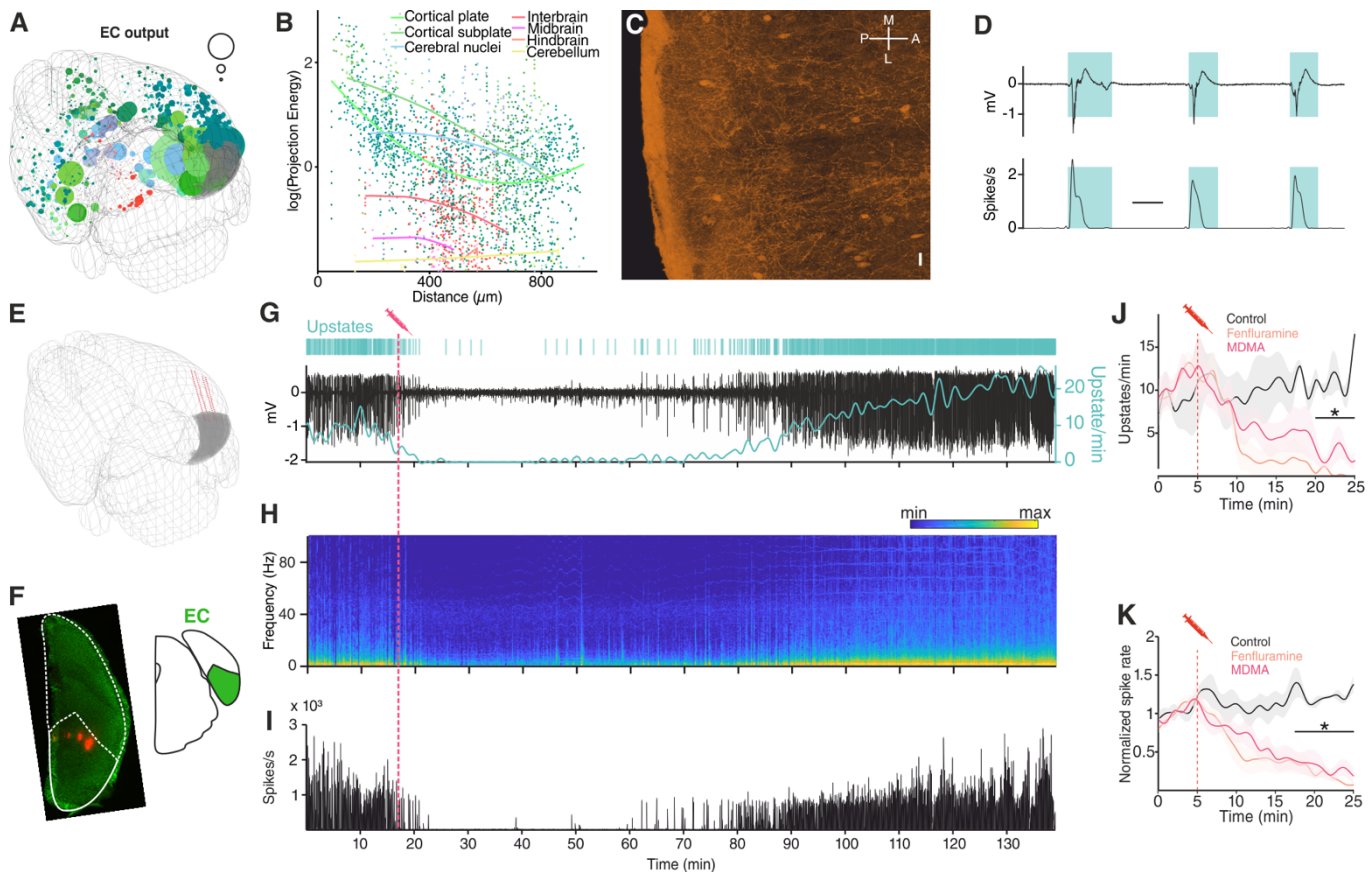
47 characterized by synchronized transitions (< 1 Hz) between periods of high activity (up-state)
48 and relative quiescence (down-state) (Steriade et al., 1993, Neske, 2015). SO are a global
49 phenomenon observed throughout the cerebral cortex and are considered to be the default
50 emergent activity of cortical networks during slow wave-sleep and anesthesia (Neske, 2015,
51 Sanchez-Vives et al., 2017). Our results show that 5-HT release *in vivo* is sufficient to suppress
52 SO and, concurrently, activate a small group of neurons characterized by an intermediate
53 waveform shape. Using cortical brain slices, we were able to characterize the 5-HT activated
54 neurons as Som-expressing interneurons and show that they are necessary mediators of the
55 effect of 5-HT on SO *in vitro*. While previous studies have shown that parvalbumin (PV)
56 interneurons are excited by 5-HT (Puig et al., 2010, Athilingam et al., 2017), our results identify
57 cortical Som interneurons as novel targets of the 5-HT neuromodulatory system.

58 **Results**

59 **5-HT inhibits SO *in vivo***

60 We investigated the effect of 5-HT on network activity in anesthetized mice using multisite
61 silicon microelectrodes placed in the entorhinal cortex (EC), a region located in the medial
62 temporal lobe interconnected to a variety of cortical and subcortical areas (Figure 1A-B, Figure
63 1-figure supplement 1) including the Raphe nuclei (Figure 1C) (van Strien et al., 2009, Muzerelle
64 et al., 2016). Under urethane anesthesia, EC, like the rest of the cortex, displays SO (Figure 1–
65 figure supplement 2). As expected, we found that up-states were present synchronously in
66 the local field potential (LFP) of all the recording channels (Figure 1–figure supplement 3) and
67 every up-state coincided with large increases in population spiking activity (Figure 1D). 5-HT
68 does not cross the blood brain barrier (Hardebo and Owman, 1980), therefore, to understand the
69 effect of 5-HT on SO we used (\pm)3,4-methylenedioxymethamphetamine (MDMA), a potent
70 presynaptic 5-HT releaser and popular recreational drug (Green et al., 2003). Intraperitoneal
71 injections of MDMA (1.25 mg/kg) caused a strong suppression of up-state incidence (Figure
72 1G-J), a decrease in power of delta frequencies (Figure 1H), and a reduction of population
73 spiking activity (Figure 1I-K). MDMA also causes, although to a lesser extent, the release of
74 dopamine and noradrenaline (Green et al., 2003). To test whether the effect of MDMA was
75 mediated specifically by 5-HT we repeated the experiment using fenfluramine (Fen) (5 mg/kg),
76 a more selective 5-HT releaser (Rothman and Baumann, 2002). Intraperitoneal injection of Fen
77 had a comparably strong suppressive effect on both the occurrence of up-states and

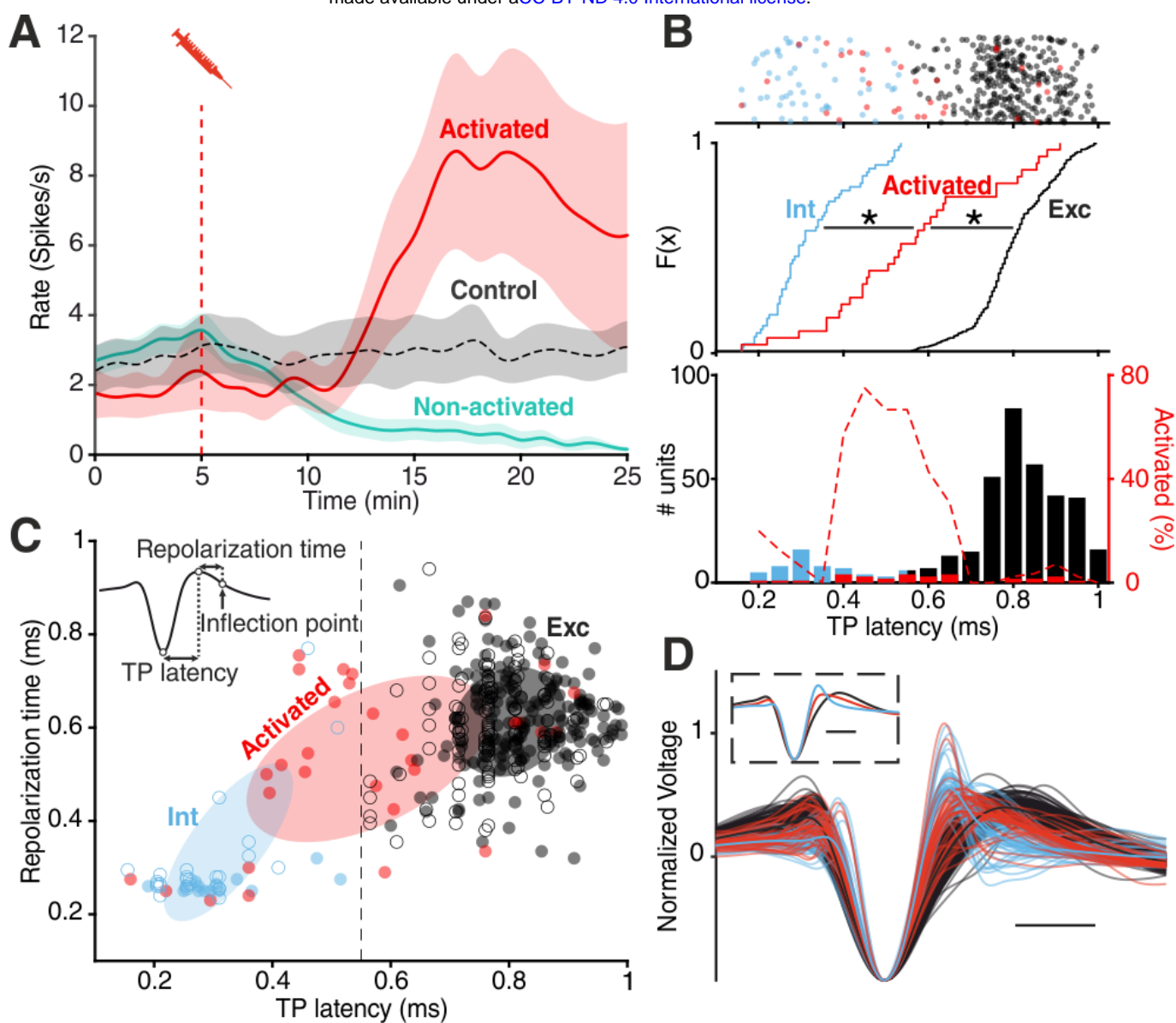
78 population spiking activity (Figure 1J-K). This shows that 5-HT released from raphe neurons
79 is capable of modulating ongoing oscillatory activity and suppress low-frequency fluctuations.



80 **Figure 1| MDMA inhibits SO in vivo.** (A) Map of EC output connectivity registered to the Allen
81 mouse common coordinate framework. Circle size represents projection energy (see
82 “Supplementary Materials and Methods”). Circle color encodes area location according to the Allen
83 institute standard: green = cerebral cortex, blue= cerebral nuclei, pink = midbrain, red =
84 interbrain/hindbrain and yellow = cerebellum. (B) Scatter plot showing relationship between
85 projection distance and projection energy. (C) Immunostaining of an ePet-YFP mouse showing
86 serotonergic fibers in medial entorhinal cortex, horizontal slice (M = medial, L = lateral, P= posterior,
87 A = anterior). Scale bar: 20 μ m. (D) LFP (top) and instantaneous population activity (bottom) of a
88 representative *in vivo* recording during SO (spikes/s units in thousands), cyan rectangles represent
89 detected up-states. (E) 3D visualization of the microelectrode location of the recording shown in g.
90 EC represented in grey. (F) Left: microelectrode tracks (red) of the recording shown in (G). Right: EC
91 position represented in green. (G) Top: Cyan lines represent detected up-states. Bottom: LFP (black)
92 and average up-state incidence per minute (cyan). Pink dotted line represents MDMA application
93 time. (H) Fourier transformation and (I) instantaneous population activity for the recording shown in
94 G (spikes/s units in thousands). (J) Mean up-state incidence after saline (control), Fen or MDMA
95 application (control: n = 5, Fen: n = 6, MDMA: n = 7; p < 10⁻⁴, unpaired t test with Holm-Sidak
96 correction). (K) Mean normalized spike rate after saline (control), Fen or MDMA application (control:
97 n = 5, Fen: n = 6, MDMA: n = 7; p < 10⁻⁴, unpaired t test with Holm-Sidak correction).

98 5-HT activates a subgroup of cortical neurons

99 Besides the LFP signal, we recorded the activity of 355 single units within the EC. Because of
100 the very similar effects of MDMA and Fen on spike rates (Figure 1K), we pooled all units
101 recorded in both types of experiments. We found that drug injections differentially affected



102
103
104
105
106
107
108
109
110
111
112
113
114
115
116

Figure 2| Divergent unit responses to MDMA/Fen application. (A) Spike rate of the activated units versus all the other units during MDMA/Fen application (activated: $n = 31$, Non-activated: $n = 324$). (B) Top: TP latencies color-coded by group. Middle: cumulative distribution of TP latencies (Kolmogorov-Smirnov test, $p_{\text{Activated vs Int}} < 10^{-4}$, $p_{\text{Activated vs Exc}} < 10^{-4}$). Bottom: bar plot representing probability distribution of TP latencies, on the right y axis dashed line representing the percentage of ‘activated’ units per TP latency bin. (C) Distribution of units according to trough-to-peak (TP) latencies and repolarization time, units were classified as putative interneurons (Int, blue) and putative excitatory (Exc, dark gray) according to a threshold at 0.55 ms; activated units (red) could belong to either group but were mostly intermediate as shown by the covariance (2 STD) of each group (Ellipses). Units recorded during control experiments are represented by empty circles. (D) Waveforms of recorded units ($n = 355$). Units were divided into “putative excitatory” (black) and “putative inhibitory” (blue) neurons according to TP latencies. Units activated either by MDMA or Fen application are represented in red. Inset shows the average waveform for each group. Scale bars: 0.5 ms.

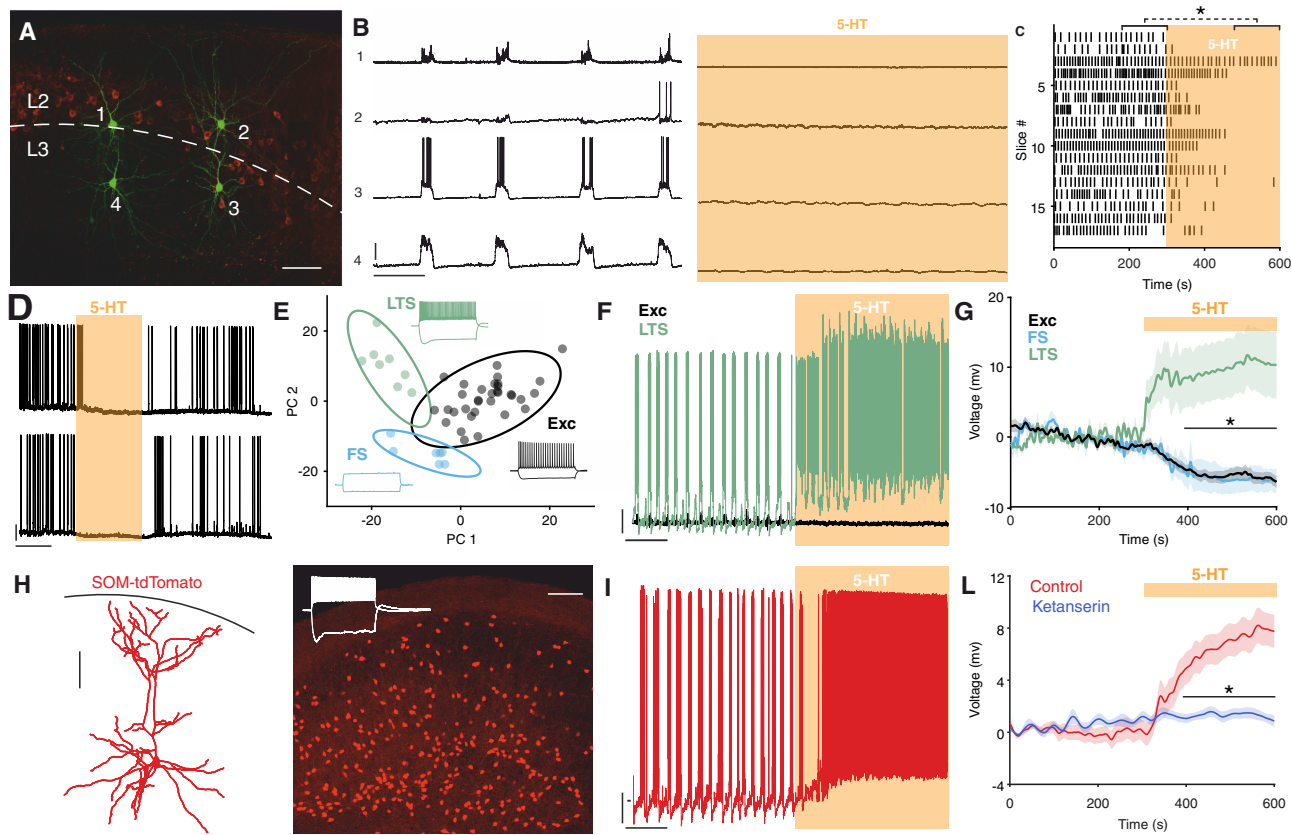
117 spiking rates (Figure 2A) of recorded units: while spiking decreased in the majority of units
118 ('non-activated'), a small group of units ('activated') responded in the opposite fashion
119 ($n=31/355$, 8.7%).

120 Trough-to-peak (TP) latency of the spike waveform has been consistently used as a metric to
121 classify units and, in accordance with previous studies (Senzai et al., 2019, Roux et al., 2014), we
122 found a clear bimodal distribution of TP latencies distinguishing putative excitatory (Exc) and
123 fast-spiking inhibitory (Int) groups. Analysis of cross-correlograms to infer monosynaptic
124 connections confirmed the inhibitory nature of a subset of putative FS units (Figure 2–figure
125 supplement 1) (Barthó et al., 2004). The cumulative distribution of TP latencies of ‘activated’
126 units was significantly different to both Exc and Int groups (Figure 2B). Specifically, the
127 average TP latency of ‘activated’ units was situated in between the Int and Exc groups (Figure
128 2B-D, Figure 2–figure supplement 2), possibly suggesting a non-fast spiking interneuron
129 identity (Trainito et al., 2019, Kvitsiani et al., 2013).

130 **5-HT suppresses SO and activates Som interneurons *via* 5-HT_{2A}R**

131 To understand the mechanism underlying the suppression of SO by 5-HT we combined
132 electrophysiology and pharmacology *in vitro*. First, we recorded simultaneously from up to
133 four neurons in the superficial layers of the EC (Figure 3A). Brain slices were perfused with an
134 extracellular solution containing Mg²⁺ and Ca²⁺ in concentrations similar to physiological
135 conditions. With this method we could reliably detect SO reminiscent of the *in vivo* network
136 activity (Tahvildari et al., 2012). Release of 5-HT *in vitro*, induced by Fen application, caused a
137 suppression of SO similar to what we observed *in vivo* (Figure 3–figure supplement 1).
138 Likewise, application of low concentrations of 5-HT (5 µM) caused a suppression of SO (Figure
139 3B, C). This effect was highly consistent across different slices and was readily reversible
140 (Figure 3D). Similarly to spontaneous up-states, electrically evoked up-states (Neske et al.,
141 2015) were also suppressed by 5-HT (Figure 3–figure supplement 2). Increasing the stimulation
142 intensity did not rescue up-state generation, indicating that lack of excitation alone cannot
143 explain the suppressive effect of 5-HT on SO.

144 Suppression of activity can have either an intrinsic or synaptic origin (Turrigiano, 2011). A
145 substantial subset of EC excitatory neurons is known to express 5-HT_{1A} receptor (5-HT_{1A}R)
146 and hyperpolarize upon 5-HT application via activation of G protein-coupled inwardly-
147 rectifying potassium (GIRK) channels (Figure 3–figure supplement 3E) (Schmitz et al., 1998,
148 Chalmers and Watson, 1991). SO suppression, however, was not influenced by blocking 5-HT_{1A}R
149 (Figure 3–figure supplement 3A, F). In contrast, blocking 5-HT_{2A}R with the selective antagonist
150 ketanserin (Preller et al., 2018) strongly reduced the suppression power of 5-HT on SO from 95
151 ± 4% to 57 ± 10.1% (Figure 3–figure supplement 3B, F). The remaining suppression can be
152 possibly explained by the activation of 5-HT_{1A}R on excitatory cells, this is reflected by the



153 **Figure 3| 5-HT suppresses SO and activates Som interneurons.** (A) Biocytin staining of
154 four simultaneously recorded cells shown in (B) WFS1 expression (in red) delimits L2/3
155 border. (B) Intracellular recordings showing synchronous up-state events in 4 simultaneously
156 recorded cells before (left) and after (right) 5-HT application. Scale bars: 1: 7.5 mV, 2: 25 mV,
157 3: 25 mV, 4: 10 mV; 10 s. (C) Up-state raster plot before and after 5-HT application, orange
158 box represents 5-HT application ($n = 17$, $p < 10^{-4}$, Wilcoxon signed rank test). (D)
159 Representative recording showing the temporary inhibitory effect of 5-HT on SO in two
160 simultaneously recorded cells. Scale bars: 5 min, 20 mV. (E) PCA projection plot of all the
161 cells recorded ($n = 48$). Cells are color coded according to group identity: Exc (black), FS
162 (light blue) or LTS (green). Typical voltage responses to current injection (-150 and +250 pA)
163 are plotted for each group. (F) Representative recording of an excitatory (black) and a low-
164 threshold (green) neuron simultaneously recorded during 5-HT application. Scale bars: 10
165 mV, 30 s. (G) Average change of RP before and after 5-HT application, across excitatory,
166 fast-spiking and low-threshold neurons (Exc: $n = 34$, FS: $n = 6$; LTS: $n = 9$; $p < 10^{-4}$, unpaired
167 t test with Holm-Sidak correction). (H) Left: Reconstruction of a recorded Som interneuron.
168 Scale bar: 100 μ m. Right: tdTomato expression in EC in a slice from a Som-tdTomato mouse.
169 Inset shows a representative Som interneuron response to current injection (-150 and +250
170 pA). Scale bar: 100 μ m. (I) Representative recording of a Som interneuron during 5-HT
171 application. Scale bars: 10 mV, 30 s. (L) Average RP of Som interneurons during 5-HT (red)
172 and ketanserin +5-HT (blue) application, orange bar represents 5-HT.

173 reduced spiking activity of putative excitatory cells (Figure 3–figure supplement 3D). Selective
174 activation of 5-HT₂R by α-methyl-5-HT could also replicate SO suppression (Figure 3–figure
175 supplement 3C, F). Together, these results point to the importance of 5-HT_{2A}R in the
176 suppression of SO.

177 5-HT_{2A}R activation causes an increase in intracellular calcium and consequent depolarization
178 of the resting potential (RP) (Nichols and Nichols, 2008). Accordingly, after 5-HT application, we
179 found that a small group of neurons was depolarized (n= 6/48, 12,5%) (Figure 3–figure
180 supplement 4). Using a soft clustering approach with six electrophysiological parameters (see
181 “Materials and Methods”) we divided the recorded cells in 3 groups: Excitatory (Exc), fast-
182 spiking (FS) and low-threshold spiking (LTS) (Figure 3E, Figure 3–figure supplement 5).
183 Strikingly, the cells excited by 5-HT belonged exclusively to the LTS group (Figure 3G, Figure
184 3–figure supplement 4).
185 A substantial part of LTS neurons expresses Som (Tremblay et al., 2016, Gibson et al., 1999),
186 therefore we performed targeted patch-clamp recordings using a mouse line expressing
187 tdTomato specifically in Som-expressing interneurons (Figure 3H). Som interneurons
188 depolarized upon 5-HT application (n=19, Δ RP: 7.5 ± 1.23 mV) (Figure 3I-L) and in some cases
189 spiked while SO were suppressed (n= 8/17, 47.05%, mean spiking rate = 3.03 ± 0.39 spikes/s).
190 This effect was blocked by ketanserin (n = 22) (Figure 3L). We confirmed the presence of 5-
191 HT_{2A}R in Som interneurons using immunohistochemistry in mice expressing EGFP under the
192 5-HT_{2A}R promoter. We found that 11.8 ± 2.9 % of the 5-HT_{2A}R positive cells in EC colocalized
193 with Som (n = 7 mice) (Figure 3–figure supplement 6). These results suggest that Som
194 interneurons might convey synaptic inhibition involved in the suppression of SO.

195 **Som interneurons mediate the suppression of SO by 5-HT**

196 To evaluate the contribution of Som interneurons to the 5-HT-mediated silencing of SO we
197 used an opto- and pharmacogenetic approach. First, we transgenically expressed
198 channelrhodopsin-2 (ChR2) in Som interneurons (Figure 4A). Light-stimulation of ChR2-
199 expressing Som interneurons in vitro suppressed SO consistently (Figure 4D-F). Expectedly,
200 up-states associated spiking was also diminished (Figure 4C, E, F). At the end of the light
201 stimulation spontaneous up-states immediately reoccurred (Figure 4G-H), in line with a critical
202 role of Som interneurons in the modulation of SO (Fanselow et al., 2008, Funk et al., 2017, Niethard
203 et al., 2018). While this experiment establishes the ability of Som interneurons to suppress SO,
204 it does not causally link Som interneuron activation to the suppression of SO induced by 5-
205 HT. Therefore, we generated a transgenic mouse line carrying a Cre-conditional expression
206 cassette of the pharmacogenetic silencer hM4Di (Figure 4–figure supplement 1) (Armbruster et
207 al., 2007). Homozygous Cre-conditional hM4Di transgenic mice and Som-Cre mice were bred
208 to obtain heterozygous Som-Cre/hM4Di offspring, which allow specific inhibition of Som
209 interneuron activity using Clozapine-N-Oxide (CNO). Following application of 5-HT we

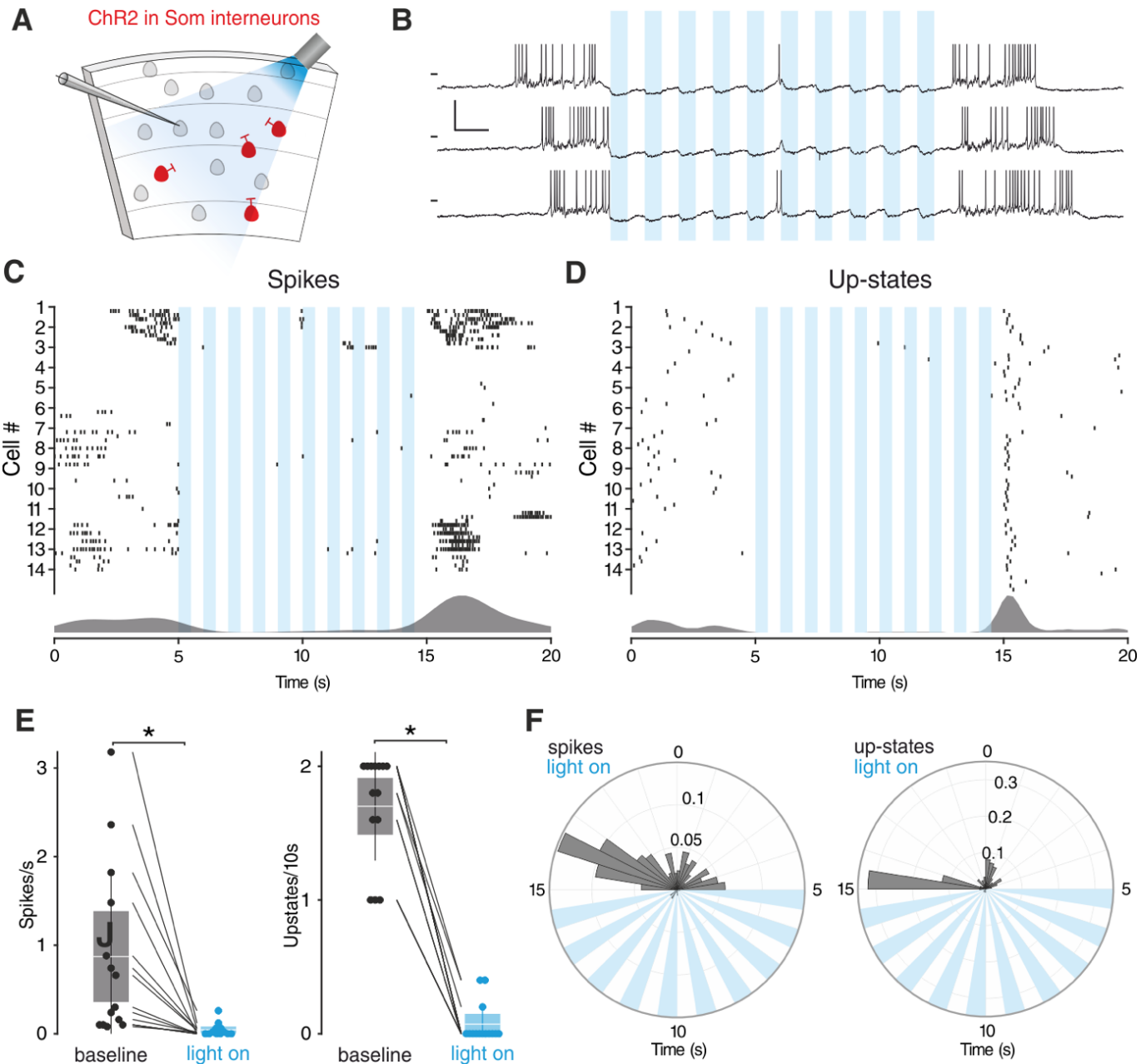
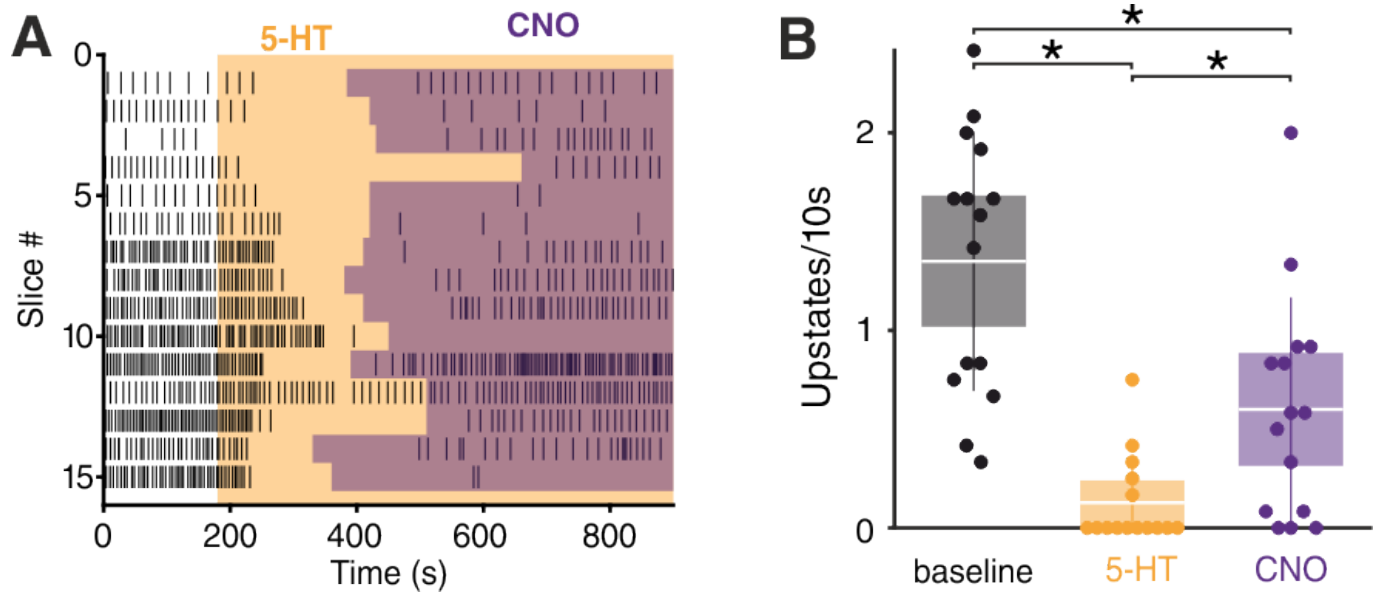


Figure 4| Som interneurons activation suppresses SO. (A) Experimental protocol: Som interneurons expressing ChR2 are activated by light during intracellular recording of layer 3 neurons in EC. (B) Representative recordings from a L3 neuron during Som interneuron activation. Scale bars: 10 mV, 0.5 s. (C) Spikes raster (top) and density plot (bottom) during light stimulation. (D) Up-state raster (top) and density plot (bottom) during light stimulation. (E) Left: spike frequency during baseline light stimulation (n=14; $p < 0.001$, Wilcoxon signed rank test). Right: Up-state incidence during baseline and light stimulation (n=14; $p < 0.001$, Wilcoxon signed rank test). Patches represent 95% confidence interval, lines represent standard deviation. (F) Left: spike probability polar plot during Som interneurons light activation. Right: up-state probability polar plot during Som interneurons light activation. Note the absence of both spiking activity and up-states during Som interneurons activation.

210
211
212
213
214
215
216
217
218
219
220

221 observed a strong reduction of up-state incidence in the LFP, which was partially restored by
222 subsequent application of CNO (Figure 5 A-B). Activation of 5-HT_{1A}R on excitatory cells and
223 the resulting decreased network excitation drive might account for the remaining suppression
224 effect of 5-HT. CNO did not show any significant effect in both wildtype littermates and

225 hM4Di-PV mice (Figure 5—figure supplement 1), indicative of the specific role played by Som
226 interneurons. In summary, while activation of Som interneurons either via 5-HT or directly by
227 ChR2 suppresses SO, the pharmacogenetic inactivation of Som interneurons weakens the
228 effect of 5-HT on SO.



229
230
231
232
233
234 **Figure 5| Som interneurons mediate the effect of 5-HT on SO.** (A) Up-state raster plot
during subsequent 5-HT and CNO application. Orange box represents 5-HT, purple boxes
represent CNO. Note the appearance of up-states after CNO application. (B) Up-state
incidence during 5-HT and 5-HT+CNO application ($n=15$; $p_{\text{baseline vs 5-HT}} < 10^{-4}$, $p_{\text{baseline vs CNO}} =$
 0.0482 , $p_{\text{5-HT vs CNO}} = 0.0405$, Kruskal-Wallis test). Patches represent 95% confidence intervals,
lines represent standard deviation.

235 Discussion

236 In this study we show that 5-HT suppresses default cortical network oscillations and, using
237 an opto- and pharmacogenetic approach, we demonstrate that Som interneurons, activated
238 by 5-HT_{2A}R, mediate this suppression in mEC.

239 Organization of cortical activity is brain state-dependent, ranging continuously from
240 “synchronized” to “desynchronized” states (Harris and Thiele, 2011). SO is on one end of this
241 continuum, representing the prototypical synchronized state. Our results, in line with previous
242 studies (Puig et al., 2010, Grandjean et al., 2019, Oikonomou et al., 2019), show that 5-HT can
243 suppress synchronized cortical activity; in addition, we identify Som interneurons as
244 necessary for this desynchronization. A parsimonious explanation that links the activation of
245 interneurons and desynchronization relies on tracking of shared input between inhibitory and
246 excitatory populations (Sippy and Yuste, 2013, Renart et al., 2010, Stringer et al., 2016): increased

247 inhibition, as shown both in computational model and experimental data, can override the
248 effect of shared input causing net decorrelation. Som interneurons, in particular, are known
249 to be sufficient to cause desynchronization in V1 (Chen et al., 2015). While it is well known that
250 Som interneurons are potently excited by acetylcholine (Chen et al., 2015, Obermayer et al., 2018,
251 Fanselow et al., 2008), our work identifies them as a novel target of 5-HT regulation via 5-HT_{2A}R.
252 The excitation of Som Interneurons by 5-HT is likely to contribute to the net inhibitory effect
253 of 5-HT release in many cortical areas (Grandjean et al., 2019, Seillier et al., 2017, Azimi et al.,
254 2020), and could explain why the inhibition strength is linearly correlated to 5-HT_{2A}R expression
255 (Grandjean et al., 2019). Giving further support to this idea, Som interneurons in motor and
256 somatosensory areas show increased cFos levels following 5-HT_{2A}R activation (Martin and
257 Nichols, 2016). Previous works have reported direct 5-HT_{2A}R dependent inhibition in prefrontal
258 cortex (PFC) (Abi-Saab et al., 1999, Ashby et al., 1990, Athilingam et al., 2017), piriform cortex
259 (Marek and Aghajanian, 1994, Sheldon and Aghajanian, 1990), cingulate cortex (Zhou and Hablitz,
260 1999), cochlear nucleus (Tang and Trussell, 2017), olfactory bulb (Petzold et al., 2009, Hardy et al.,
261 2005), visual cortex (Michaels et al., 2019, Azimi et al., 2020) and hippocampus (Wyskiel and
262 Andrade, 2016). However, none of these studies identified interneurons using molecular
263 markers and we do not exclude that different interneuron classes in other cortical areas might
264 mediate the inhibitory downstream effects of 5-HT_{2A}R. For example, in PFC a subgroup of PV
265 interneurons has been reported to be activated by this receptor (Athilingam et al., 2017, Puig et
266 al., 2010).

267 5-HT modulation is also involved in gain regulation. In olfactory cortex, 5-HT has a selective
268 subtractive effect on stimulus evoked firing (Lottem et al., 2016), and a recent work has shown
269 in visual cortex that the reduced gain of evoked responses is dependent on 5-HT_{2A}R activation
270 (Azimi et al., 2020). Intriguingly, Som interneurons have been shown to regulate subtractive
271 inhibition (Sturgill and Isaacson, 2015, Wilson et al., 2012).

272 Beside its involvement in various physiological brain processes, 5-HT is also associated with
273 the etiology of various psychiatric disorders and the same applies for Som interneurons
274 (Pantazopoulos et al., 2017, Lin and Sibille, 2015). 5-HT is also linked to the psychological effect
275 of many psychotropic drugs. Most interestingly, 5-HT_{2A}R activation is essential for the
276 psychological effects induced by various psychedelics (Nichols, 2016) and, in the case of
277 MDMA, has been linked to perceptual and emotional alterations (Liechti et al., 2000, Kuypers et
278 al., 2018). Broadband reduction in oscillatory power, triggered by 5-HT_{2A}R, seems to be linked
279 to the subjective effect of serotonergic drugs (Carhart-Harris et al., 2016, Carhart-Harris and
280 Friston, 2019) and it has been consistently observed in humans and rodents following

281 administration of MDMA (Frei et al., 2001, Lansbergen et al., 2011) or various other 5-HT_{2A}R
282 agonists (Kometer et al., 2015, Muthukumaraswamy et al., 2013, Carhart-Harris et al., 2016, Wood et
283 al., 2012). The link between 5-HT_{2A}R and perception is further supported by the fact that a
284 number of routinely used antipsychotic drugs are potent 5-HT_{2A}R antagonists (Marek et al.,
285 2003, Meltzer, 1999). While the most recent attempts to explain the psychological effects of 5-
286 HT_{2A}R activation focus on the increased spiking of cortical pyramidal neurons in the deep
287 layers (Carhart-Harris and Friston, 2019, Nichols, 2016), our study suggests that Som interneurons
288 may also play a role. Som interneurons, in contrast to PV interneurons, biasedly form
289 synapses on the dendrites of their target cell (Tremblay et al., 2016). A wealth of evidence
290 suggests that active dendritic processing in cortical pyramidal neurons has a critical influence
291 on sensory perception (Takahashi et al., 2016, Murayama et al., 2009, Smith et al., 2013,
292 Ranganathan et al., 2018) and, in accordance to their unique anatomical properties, Som
293 interneurons strongly influence dendritic computations and directly modulate perceptual
294 thresholds (Takahashi et al., 2016). We propose that the novel link between 5-HT_{2A}R and Som
295 interneurons might help elucidate the mechanism underlying a host of psychiatric disorders
296 and contribute to our understanding of how serotonergic drugs exert their psychological
297 effects.

298

299 **Materials and Methods**

300 All experiments were conducted according to regulations of the Landesamt für Gesundheit
301 und Soziales (Berlin [T 0100/03], Berlin [G0298/18]) and the European legislation (European
302 Directive 2010/63/EU).

303 **Animals**

304 Data for the *in vivo* part of the study were collected from C57BL6 mice (aged 6 to 10 weeks).
305 Data for the *in vitro* part were collected from C57BL6 (P10-P17), Som-tdtomato (P10-P30),
306 Sst-Chr2-EYFP (P10-P16), hM4Di-Som (P10-P15), hM4Di-Som (+/-) (P10-P15) and hM4Di-
307 PV (P10-P15) mice. Immunostainings to localize 5-HT_{2A}R were performed on 5-HT_{2A}R-EGFP
308 mice (P20-P90) and Immunostainings to localize 5-HT fibers (Fig.1 c) were performed on an
309 ePet-YFP mouse (P35). The animals were housed in a 12:12 hours light-dark cycle in singularly
310 ventilated cages with *ad libitum* access to food and water. SO *in vitro* recordings were
311 performed on P12-P16 mice.

312 **Drugs**

313 Urethane (U2500, Sigma), fenfluramine ((+)-Fenfluramine hydrochloride, F112, Sigma), 5-HT
314 (Serotonin creatinine sulfate monohydrate, H7752, Sigma), WAY-100635 (W108, Sigma), α-
315 Methylserotonin (α-Methylserotonin maleate salt, M110, Sigma) MDMA ((±)3,4-
316 methylenedioxymethamphetamine, 64057-70-1, Sigma), CNO (Clozapine *N*-oxide
317 dihydrochloride, 6329, Tocris) were dissolved in water for *in vitro* application and in 0.9%
318 normal saline for *in vivo* application. Ketanserin (Ketanserin (+)-tartrate salt, S006, Sigma) was
319 dissolved in Dimethyl sulfoxide (DMSO).

320 **Surgery and *in vivo* recording**

321 Mice were briefly anaesthetized with isofluorane (2%) and then injected intraperitoneally with
322 urethane (1,2 g/kg, Sigma Aldrich, Munich, Germany). The level of anesthesia was maintained
323 so that hindlimb pinching produced no reflex movement and supplemental doses of urethane
324 (0.2 g/kg) were delivered as needed. Upon cessation of reflexes the animals were mounted
325 on a stereotaxic frame (Kopf Instruments, Tujunga, California), and body temperature was
326 maintained at 38°C. The scalp was removed, and the skull was cleaned with saline solution.
327 A craniotomy was performed at +3 mm ML, -3 mm AP, +3.25 mm DV.

328 Extracellular recordings from EC were performed using a Cambridge Neurotech 64-channels
329 (n = 15) or 32-channels (n = 3) silicon probe. The recording electrode was painted with the
330 fluorescent dye Dil (Thermo Fisher Scientific, Schwerte, Germany) and then slowly lowered
331 into the craniotomy using micromanipulators (Luigs&Neumann, Ratingen, Germany) at a 25°
332 angle AP (toward the posterior side of the brain). The exposed brain was kept moist using
333 saline solution. A ground wire connected to the amplifier was placed in the saline solution
334 covering the skull to eliminate noise. Brain signals were recorded using a RHD2000 data
335 acquisition system (Intan Technologies, Los Angeles, California) and sampled at 20kHz.
336 Recording quality was inspected on-line using the open-source RHD2000 Interface Software.
337 Recordings began after a 10-minute waiting period in which clear Up-states could
338 consistently be seen at a regular frequency.

339 ***In vivo analysis***

340 We selected the channel to use for up-state detection based on the standard deviation (STD)
341 of the trace during baseline (first 5 minutes of recording), the channel with the highest STD
342 was selected as larger voltage deflection increases detection algorithm accuracy. Given the
343 highly synchronous nature of SO (Supplementary Fig. 3) the spatial location of the channel
344 selected was not considered. Up-states were detected comparing threshold crossing points
345 in two signals: the delta-band filtered signal (0.5-4 Hz) and the population spike activity.
346 Candidate up-states were identified in the delta-band filtered signal using two dynamic
347 thresholds 'a' and 'b':

$$348 \quad a = m + \frac{\sigma}{1.5}$$
$$349 \quad b = m + \frac{\sigma}{0.8}$$

350 Where σ is the standard deviation of the signal during the first five minutes of recording
351 (baseline) and m is the centered moving median calculated using 60 s windows (Matlab
352 function *movmedian*). The median was used instead of the mean to account for non-
353 stationaries in the data. A candidate up-state was identified at first using the threshold
354 crossings of the signal compared to 'a': candidates shorter than 200 ms were deleted and
355 candidates happening in a window of 300 ms were joined together. Subsequently the
356 threshold 'b' was used to separate up-states occurring in close proximity: if the signal within
357 one candidate crossed the threshold 'b' in more than one point then the candidate up-state
358 was split in two at the midpoint between the two threshold crossings. Candidate up-states

359 were finally confirmed if the population spike activity (calculated in 100 ms windows) within
360 the candidate crossed a threshold of 1σ (calculated during the baseline).

361 **Units detection and classification**

362 Spike detection was performed offline using the template-based algorithm Kilosort2
363 (<https://github.com/MouseLand/Kilosort2>), with the following parameters:

- 364 ▪ ops.fshigh = 300
- 365 ▪ ops.fsslow = 8000
- 366 ▪ ops.minfr_goodchannels = 0
- 367 ▪ ops.Th = [8 4]
- 368 ▪ ops.lam = 10
- 369 ▪ ops.AUCsplit = 0.9
- 370 ▪ ops.minFR = 1/1000
- 371 ▪ ops.momentum = [20 400]
- 372 ▪ ops.sigmaMask = 30
- 373 ▪ ops.ThPre = 8
- 374 ▪ ops.spkTh = -6
- 375 ▪ ops.nfilt_factor = 8
- 376 ▪ ops.loc_range = [3 1]
- 377 ▪ ops.criterionNoiseChannel = 0.2
- 378 ▪ ops.whiteningrange = 32
- 379 ▪ ops.ntbuff = 64

380 Manual curation of the results was performed using Phy (<https://github.com/cortex-lab/phy>).
381 Each Isolated unit satisfied the following two criteria: Refractory period (2 ms) violations < 5%,
382 fraction of spikes below detection threshold (as estimated by a gaussian fit to the distribution
383 of the spike amplitudes) < 15%. Units with negative maximal waveform amplitude were further
384 classified as putative excitatory if the latency (TP latency) was ≥ 0.55 ms or putative inhibitory
385 when TP latency < 0.55 ms. The value 0.55 was chosen in accordance with previous works
386 (Senzai et al., 2019, Antoine et al., 2019). Pharmacological classification: units were classified as
387 'activated' if their firing rate in the 25 minutes following drug injection was 2σ (standard
388 deviation) above the baseline rate for at least 5 minutes. Remaining units were pulled together
389 in the category 'non-activated'.

390 **Cross-correlogram analysis**

391 Cross-correlogram based connectivity analysis was performed for every unit to identify
392 inhibitory connections. Units with a spiking rate smaller than 0.3 spikes/s were discarded from
393 the analysis. We used total spiking probability edges (TPSE) algorithm
394 (<https://github.com/biomemsLAB/TSPE>) (De Blasi et al., 2019) to identify in a computationally
395 efficient manner putative inhibitory connections between units and all clusters recorded. The
396 parameters used were:

397

398

- $d = 0$,
- $\text{neg_wins} = [2, 3, 4, 5, 6, 7, 8]$,
- $\text{co_wins} = 0$,
- $\text{pos_wins} = [2, 3, 4, 5, 6]$,
- $\text{FLAG_NORM} = 1$.

403

404 The connectivity vectors of each unit resulting from TSPE were sorted by inhibition strength.
405 Top 20 connections were further analyzed using custom Matlab code. A connection was
406 classified as inhibitory if the cross correlogram values (x) were smaller than the mean of x by
407 more than one standard deviation ($x < \text{mean}(x) - \text{std}(x)$) in at least 4 consecutive bins (bin size
408 = 1 ms) in a window 4 to 9 ms after the center of the cross-correlogram.

409 **Slice preparation**

410 We prepared acute near horizontal slices ($\sim 15^\circ$ off the horizontal plane) of the medial
411 entorhinal cortex (mEC) from C57Bl6/n mice. Animals were decapitated following isoflurane
412 anesthesia. The brains were quickly removed and placed in ice-cold ($\sim 4^\circ \text{ C}$) ACSF (pH 7.4)
413 containing (in mM) 85 NaCl, 25 NaHCO₃, 75 Sucrose, 10 Glucose, 2.5 KCl, 1.25 NaH₂PO₄,
414 3.5MgSO₄, 0.5 CaCl₂, and aerated with 95% O₂, 5% CO₂. Tissue blocks containing the brain
415 region of interest were mounted on a vibratome (Leica VT 1200, Leica Microsystems), cut at
416 400 μm thickness, and incubated at 35 $^\circ\text{C}$ for 30 min. The slices were then transferred to
417 ACSF containing (in mM) 85 NaCl, 25 NaHCO₃, 75 Sucrose, 10 Glucose, 2.5 KCl, 1.25
418 NaH₂PO₄, 3.5 MgSO₄, 0.5 CaCl₂. The slices were stored at room temperature in a
419 submerged chamber for 1-5 hr before being transferred to the recording chamber.

420 ***In vitro* recording**

421 In order to perform whole-cell recordings slices were transferred to a submersion style
422 recording chamber located on the stage of an upright, fixed-stage microscope (BX51WI,
423 Olympus) equipped with a water immersion objective (x60, Olympus) and a near-infrared
424 charge-coupled device (CCD) camera. The slices were perfused with ACSF (~35 °C bubbled
425 with 95 % O₂-5 % CO₂) at 3-5 ml/ min to maintain neuronal health throughout the slice. The
426 ACSF had the same composition as the incubation solution except for the concentrations of
427 calcium and magnesium, which were reduced to 1.2 and 1.0 mM, respectively. Recording
428 electrodes with impedance of 3-5 MΩ were pulled from borosilicate glass capillaries (Harvard
429 Apparatus, Kent, UK; 1.5 mm OD) using a micropipette electrode puller (DMZ Universal Puller).
430 The intracellular solution contained the following (in mM): 135 K-gluconate, 6 KCl, 2 MgCl₂,
431 0.2 EGTA, 5 Na₂- phosphocreatine, 2 Na₂-ATP, 0.5 Na₂-GTP, 10 HEPES buffer, and 0.2%
432 biocytin. The pH was adjusted to 7.2 with KOH. Recordings were performed using Multiclamp
433 700A/B amplifiers (Molecular Devices, San Jose, California). The seal resistance was >1 GΩ.
434 Capacitance compensation was maximal and bridge balance adjusted. Access resistance
435 was constantly monitored. Signals were filtered at 6 kHz, sampled at 20 kHz, and digitized
436 using the Digidata 1550 and pClamp 10 (Molecular Devices, San Jose, California). Activation
437 light was delivered by a 460 nm laser (DPSS lasers, Santa Clara, California) using a 460–480
438 nm bandpass excitation filter. Stimulation consisted of 500 ms pulses at 1 Hz.
439 Stimulation experiments were performed using a bipolar micro-electrode (glass pipette filled
440 with ACSF solution, wrapped by a fine grounding wire) connected to an isolated voltage
441 stimulator (ISO-Flex, A.M.P.I., Israel). A 4x objective (Olympus) was used to visually guide the
442 stimulating electrode into the mEC. Stimulation power was adjusted to achieve consistent up-
443 state generation during baseline (> 95%). Each stimulus had a duration of 50 µs, inter-stimuli
444 interval was 8-10 seconds.

445 **In vitro analysis**

446 *In vitro* up-states were detected in Matlab using an algorithm similar to the one described in
447 the *in vivo* analysis method section. We used a coincident detection in two signals. In
448 multicellular recordings we used the membrane potential of 2 cells, in single cell recording we
449 used membrane potential and the envelope of the gamma filtered trace (50-250 Hz), as up-
450 states are characterized by an increase in gamma activity (Neske, 2015).
451 Baseline condition was calculated using the last 120 s before drug application, post-drug
452 application condition was calculated using the last 120 s of recording after drug application
453 (Total recording duration: 600 s).

454 Excitatory (Exc), fast spiking (FS) and low-threshold spiking (LTS) neurons were classified
455 using Gaussian mixture models (GMM) with a soft clustering approach in Matlab. Input
456 resistance (R_{in}), Δ after-hyperpolarization (ΔAHP), sag, rheobase, spike width and resting
457 potential (RP) were extracted from each neuron and used in the classification. The first two
458 components of the principal component analysis (PCA) were used to fit the data to a Gaussian
459 mixture model distribution. Initial values were set according to the k-means algorithm with
460 centroid positioned at x and y position: 5, 0; -15, -15; -15, 10. This centroid were placed
461 according to the loadings of the PCA to identify 3 clusters with the following main features:

462 ▪ Cluster 1 (putative Exc): high spike width, low AHP, low rheobase.
463 ▪ Cluster 2 (putative FS): low spike width, low SAG, high rheobase, low R_{in} .
464 ▪ Cluster 3 (putative LTS): low spike width, high SAG, high AHP, high R_{in} .

465 Covariance matrices were diagonal and not shared. Neurons with a posterior probability of
466 belongings to any of the three clusters < 90% were discarded from further analysis (1/49).
467 While the majority of Som-interneurons display LTS features, a minority (~10%) belongs to
468 the FS group (Urban-Ciecko et al., 2015). To distinguish FS and LTS interneurons in the SOM-
469 Td Tomato mice we employed the GMM with posterior probability threshold of 90%.

470 **Inter-area connectivity analysis**

471 Projection data was downloaded from the from the Allen Mouse Brain Connectivity Atlas via
472 the provided API (application programming interface) using freely available code
473 (<https://github.com/SainsburyWellcomeCentre/AllenBrainAPI>). Different connectivity metrics
474 are provided for each experiment:

475

476 • Normalized projection volume =
$$\frac{\text{Projection volume}}{\text{Total volume of signal in injection site}}$$

477 • Projection density =
$$\frac{\text{Number of pixels identified as projecting in the structure}}{\text{Number of valid pixels in the structure}}$$

478 • Projection intensity =
$$\frac{\text{Sum of intensity values in projecting pixels in the structure}}{\text{Number of pixels identified as projecting in the structure}}$$

479 • Projection energy =
$$\frac{\text{Projection density}}{\text{projection intensity}}$$

480

481 We chose to use projection energy as it directly relates signal strength (pixel intensity) to the
482 size of a give structure (total number of pixels in the structure), in this case a widely spread

483 weak signal and a narrow strong signal may both have similar projection energies. Projection
484 energy was normalized across different experiments dividing by the injection volume.
485 Projection signal in injection area was excluded. More information about the record properties
486 can be found on the Allen SDK (software development kit) website
487 <https://alleninstitute.github.io/AllenSDK/unionizes.html>. Each annotation was assigned a new
488 additional structure ID to enable the calculation of average projection energy per area.
489 Entorhinal cortex (EC) output was calculated combining the results of experiments 114472145
490 (injection site: lateral EC) and 113226232 (injection site: medial EC).
491 Connectivity analysis was performed using custom Matlab (2018a) code, the code is available
492 on Github (<https://github.com/RobertoDF/BRIO>).

493 **Generation of Cre-conditional hM4Di mice**

494 We produced a transgenic mouse line carrying a Cre-conditional hM4Di expression cassette
495 in the Rosa26 locus. The transgene construct was inserted by recombination-mediated
496 cassette exchange (RMCE). RMCE relies on recombination events between attB and attP
497 recognition sites of the RMCE plasmid and genetically modified acceptor embryonic stem
498 (ES) cells, mediated by the integrase of phage phiC31(Hitz et al., 2007). The RMCE construct
499 is thereby shuttled into the Rosa26 locus of the ES cells, along with a Neomycin resistance
500 cassette (fig. S12A). The acceptor cell line IDG3.2-R26.10-3 (I3) was kindly provided by Ralf
501 Kühn (GSF National Research Centre for Environment and Health, Institute of Developmental
502 Genetics, Neuherberg, Germany).
503 We subcloned a Cre-conditional FLEX (flip-excision) cassette (Schnutgen et al., 2003) into
504 pRMCE, and inserted a strong CAG promoter (CMV immediate early enhancer/modified
505 chicken β-actin promoter, from Addgene Plasmid #1378) in front of the FLEX-cassette to
506 create pRMCE-CAG-Flex. The coding sequence of hM4Di-mKateT was inserted into the FLEX
507 cassette in reverse orientation to the promoter (fig. S12A). Finally, a rabbit globulin polyA
508 cassette including stop codons in every reading frame was placed downstream of the FLEX
509 cassette, in the same direction as hM4Di, in order to prevent unintended transcriptional read-
510 through from potential endogenous promoters. The construct was completely sequenced
511 before ES cell electroporation.

512 Electroporation of the RMCE construct together with a plasmid encoding C31int was
513 performed by the transgene facility of the ‘Research Institute for Experimental Medicine’ (FEM,
514 Charité, Berlin) according to published protocols (Hitz et al., 2009, Hitz et al., 2007). Recombinant
515 clones were selected by incubation with 140 µg/ml G418 for at least 7 days. To activate hM4Di

516 expression by recombination of the FLEX switch, selected clones were further transfected
517 transiently with pCAG-Cre-EGFP using Roti-Fect (Carl Roth, Karlsruhe, Germany). G418-
518 resistant clones were analyzed by PCR for successful integration and recombination of the
519 construct (fig. S12B), using the following primer:
520 GT001 PGK3'-fw: CACGCTTCAAAAGCGCACGTCTG;
521 GT002 Neo5'-rev: GTTGTGCCAGTCATAGCCGAATAG;
522 GT005 PolyA-fw: TTCCTCCTCTCCTGACTACTCC;
523 GT006 Rosa3'-rev: TAAGCCTGCCAGAAGACTC;
524 GT013 hM4Di3'rev: CAGATACTGCGACCTCCCTA
525 After verification of correct integration and functional FLEX-switch recombination, we
526 generated chimeras by blastocyst injection of I3 ES cells. Heterozygous offsprings were
527 mated with a Flpe deleter mouse line in order to remove the neomycin resistance cassette by
528 Flp-mediated recombination.
529 Mice homozygous for the Rosa-CAG-FLEX-hM4Di-mKateT allele are viable and fertile and
530 show now obvious phenotype. Importantly, application of CNO to these mice does not induce
531 any behavioral effects. Homozygous Cre-conditional hM4Di transgenic mice and Som-Cre
532 mice (Taniguchi et al., 2011) were maintained on a C57BL/6n genetic background and were
533 bred to obtain heterozygous Som-Cre / hM4Di offsprings.

534 **Histological analysis**

535 For the *post-mortem* electrode tracks reconstructions of the *in vivo* recordings, mice were not
536 perfused, brain were extracted from the skull, post-fixed in 4% PFA overnight at 4°C and
537 afterwards cut with a vibratome (Leica Microsystems, Wetzlar Germany) in 100 µM thick
538 sequential sagittal slices. Images were taken using a 1.25x objective and stitched together
539 using the microscope software (BX61, Olympus), afterwards we used AllenCCF code
540 (<https://github.com/cortex-lab/allenCCF>) to identify electrode shanks location (Shamash et al.,
541 2018).
542 For the anatomical reconstructions of recorded cells *in vitro* brain slices were fixed with 4%
543 paraformaldehyde in 0.1 M phosphate buffer (PB) for at least 24 hours at 4°C. After being
544 washed three times in 0.1 M PBS, slices were then incubated in PBS containing 1% Triton X-
545 100 and 5% normal goat serum for 4 hr at room temperature (RT). To visualize biocytin-filled
546 cells we used Streptavidin Alexa 488 conjugate (1:500, Invitrogen), WFS1 (1:1000, Rabbit,
547 Proteintech, IL, USA) was used in a subset of analysis to visualize the L2/L3 border, Som
548 (1:1000, Rat, Bachem, Switzerland) was used in the 5-HT_{2A}R localization analysis. Slices were

549 incubated with primary antibodies for 48 hours at RT. After rinsing two times in PBS, sections
550 were incubated in the PBS solution containing 0.5% Triton X-100, Alexa fluor 488, Alexa fluor
551 555 and Alexa fluor 647 (Invitrogen Corporation, Carlsbad, CA) according to the number of
552 antibodies used. Slices were mounted in Fluoroshield (Sigma-Aldrich) under coverslips 2-3 hr
553 after incubation with the secondary antibodies and stored at 4 °C.
554 Labeled cells were visualized using 20x or 40x objectives on a confocal microscope system
555 (SP8, Leica). For the 5-HT_{2A}R localization analysis images of the whole EC were acquired and
556 stitched together using the auto stitching method, with smoothing set to off. Z stacks were
557 acquired every 30 µM. The Image stacks obtained were registered and combined in Fiji
558 (<http://fiji.sc/wiki/index.php/Fiji>) to form a montage of the sections. Cell counting was
559 executed using Fiji multi-point tool. X-Y-Z coordinates of each 5-HT_{2A}R-EGFP positive cell
560 were exported to Matlab and subsequently, using custom written code in Matlab, we semi-
561 automatically inspected each cell for colocalization between EGFP(5-HT_{2A}R) and Som.

562 Statistical Analysis

563 All datasets were tested to determine normality of the distribution either using D'Agostino-
564 Pearson omnibus normality test or Shapiro-Wilk normality test. Student's t-test and one-way
565 ANOVA were used for testing mean differences in normally distributed data. Wilcoxon
566 matched-pairs signed rank test and Kruskal-Wallis were used for non-normally distributed
567 datasets. Dunn-Sidak multiple comparison test was used to compare datasets with 3 or more
568 groups. Kolmogorov-Smirnov test was used to compare cumulative distributions. Statistical
569 analysis was performed using Prism (6.01) and Matlab (2019a).
570 All data are expressed as mean ± SEM Asterisks in figures represents p-values smaller than
571 0.05 unless stated otherwise in the legend.

572 Data and code availability

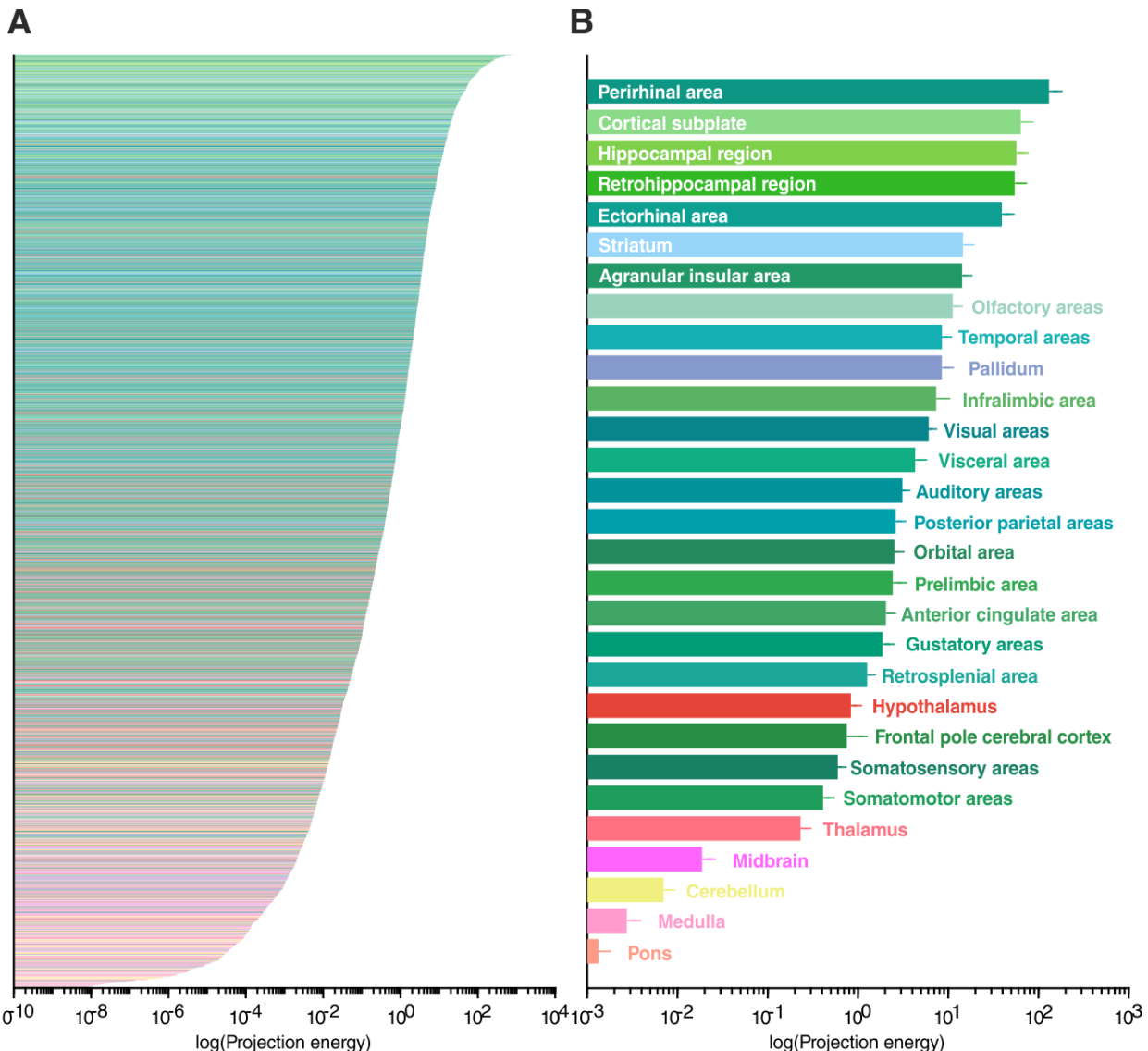
573 The code generated during this study is available from the corresponding author upon
574 reasonable request.

575 **Acknowledgments:** We thank A. Schönherr, S. Rieckmann, K. Czieselzky, A. Fortströer, A.R.
576 Sammons, M. Brecht, M. E. Larkum.

577 **Author contributions:** Conceptualization: R.D.F. and D.S.. Methodology: J.J.T., P.B., R.D.F
578 and B.R.. Investigation: R.D.F, A.S., C.C. and P.B. Software and formal analysis: R.D.F..

579 Resources: P.B. and C.H.. Supervision: D.S.. Project administration: R.D.F., D.S.. Funding
580 acquisition: D.S.. Original draft preparation: R.D.F. and D.S. Review and editing: all authors.
581

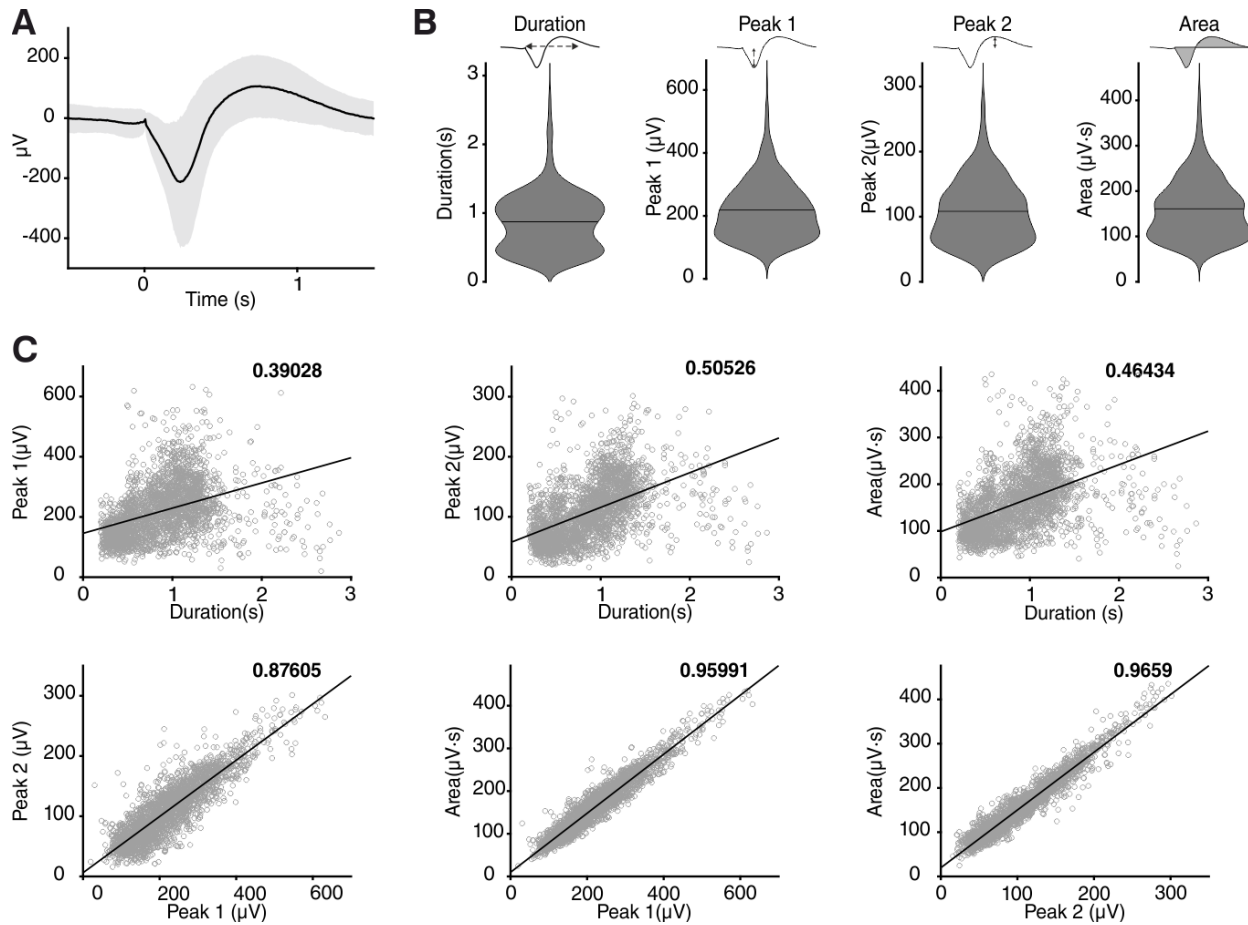
582 **Supplementary Figures**



583 **Figure 1–figure supplement 1. Regional output connectivity of EC.**

584 (A) Projection energy of all identified EC outputs color coded according to Allen institute
585 standard: green = cerebral cortex, blue= cerebral nuclei, pink = midbrain, red =
586 interbrain/hindbrain and yellow = cerebellum. (B) Same data as (A) consolidated in higher level
587 regions.

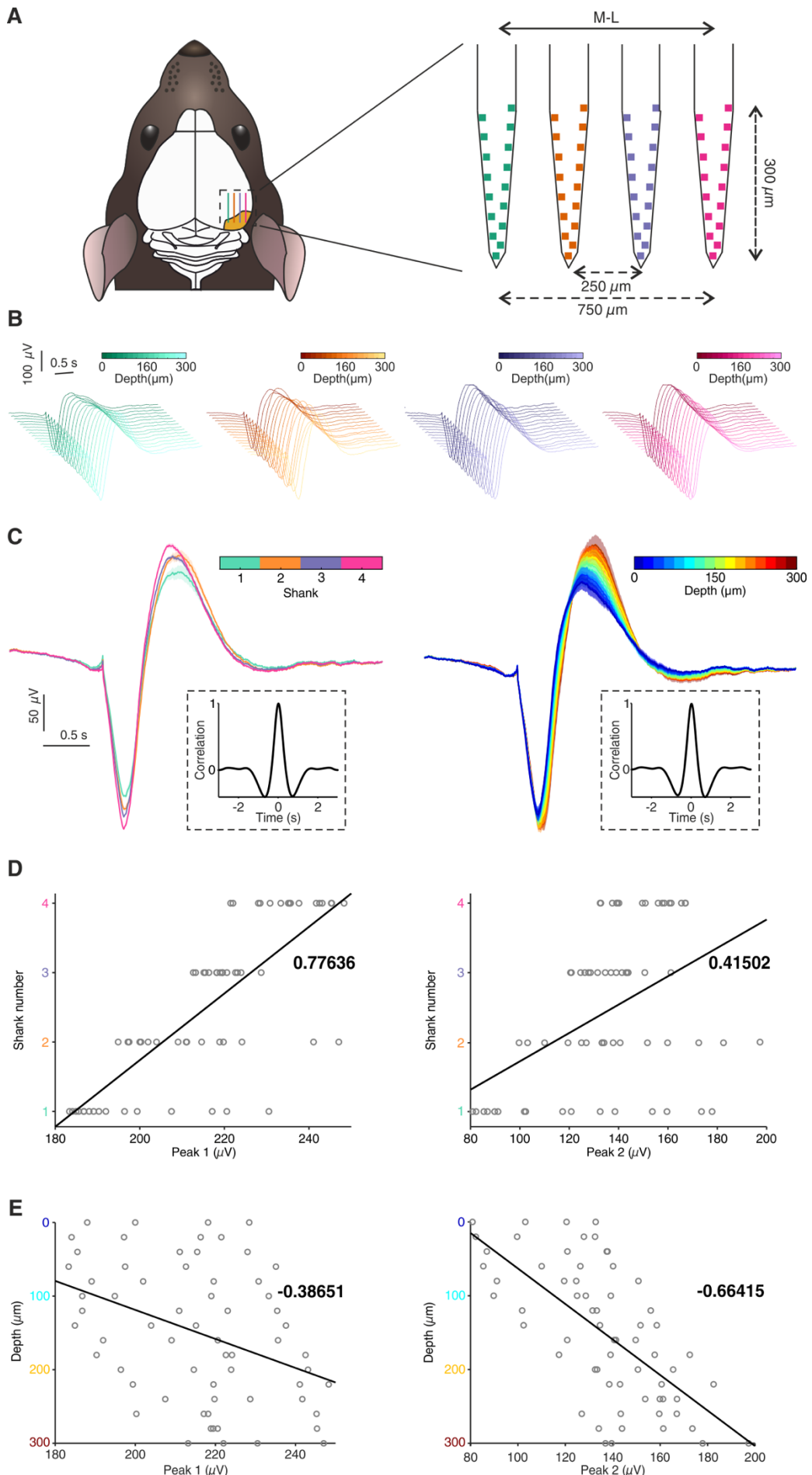
588



589 **Figure 1-figure supplement 2. *In vivo* up-state metrics.**

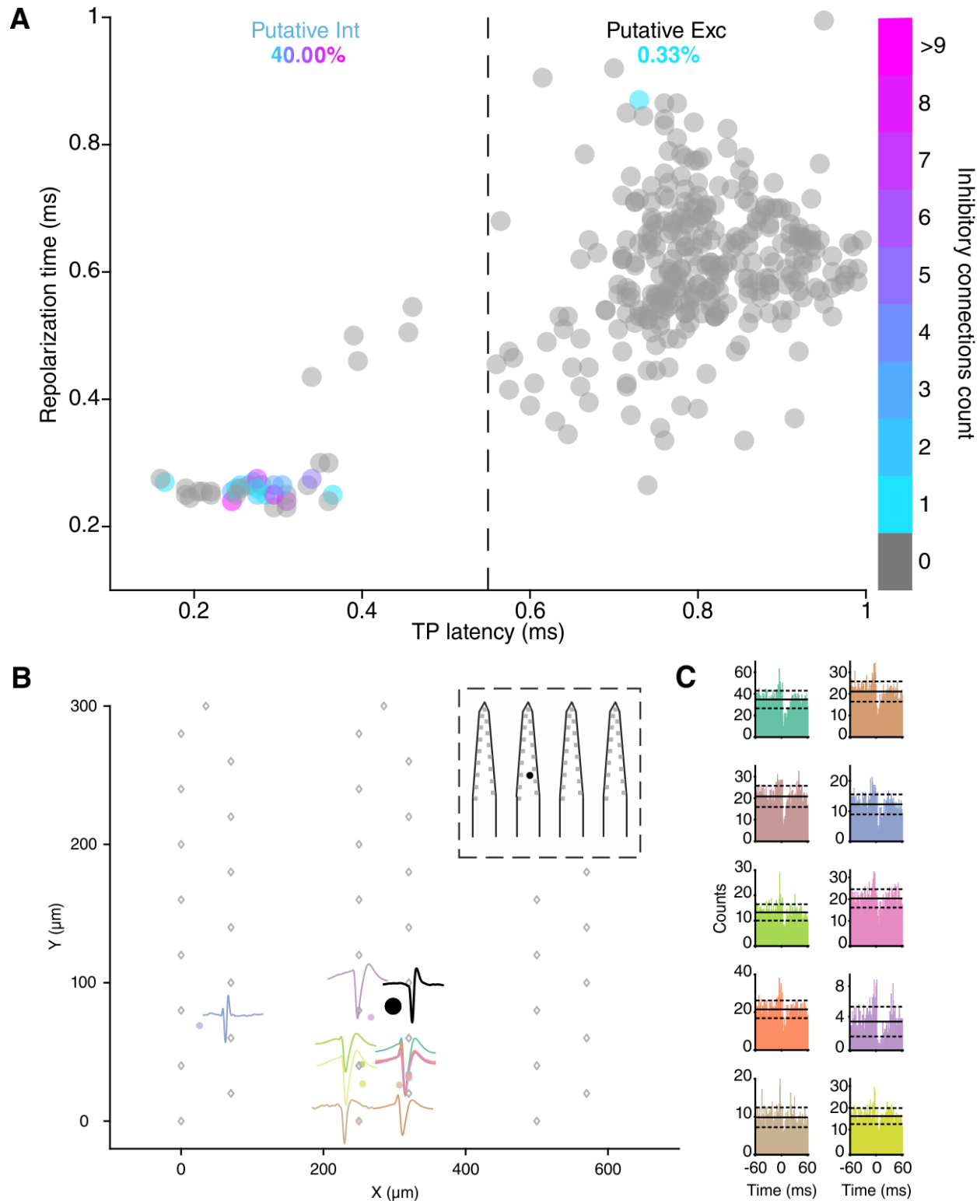
590 **(A)** Average up-state voltage deflection, grey patch represents 1 standard deviation (n_{detected}
591 up-states = 2655, $n_{\text{animals}} = 18$). For each recording the channel with the biggest voltage deflection
592 was selected, see “Methods”. For experiments with drug application (either MDMA or Fen)
593 only baseline up-states were taken in account. **(B)** Violin plots of duration (mean: 0.87 ± 0.008
594 s), peak 1 amplitude (mean: $218.59 \pm 1.83 \mu\text{V}$), peak 2 amplitude (mean: $108.27 \pm 0.97 \mu\text{V}$)
595 and area (mean: $160.88 \pm 1.31 \mu\text{V}\cdot\text{s}$) of each detected up-state. **(C)** Scatter plots showing
596 relationships between metrics used in (B). Bold black number in each plot represent the
597 correlation coefficient ($p < 0.001$).

598



599 **Figure 1–figure supplement 3. *In vivo* up-state spatial features.**

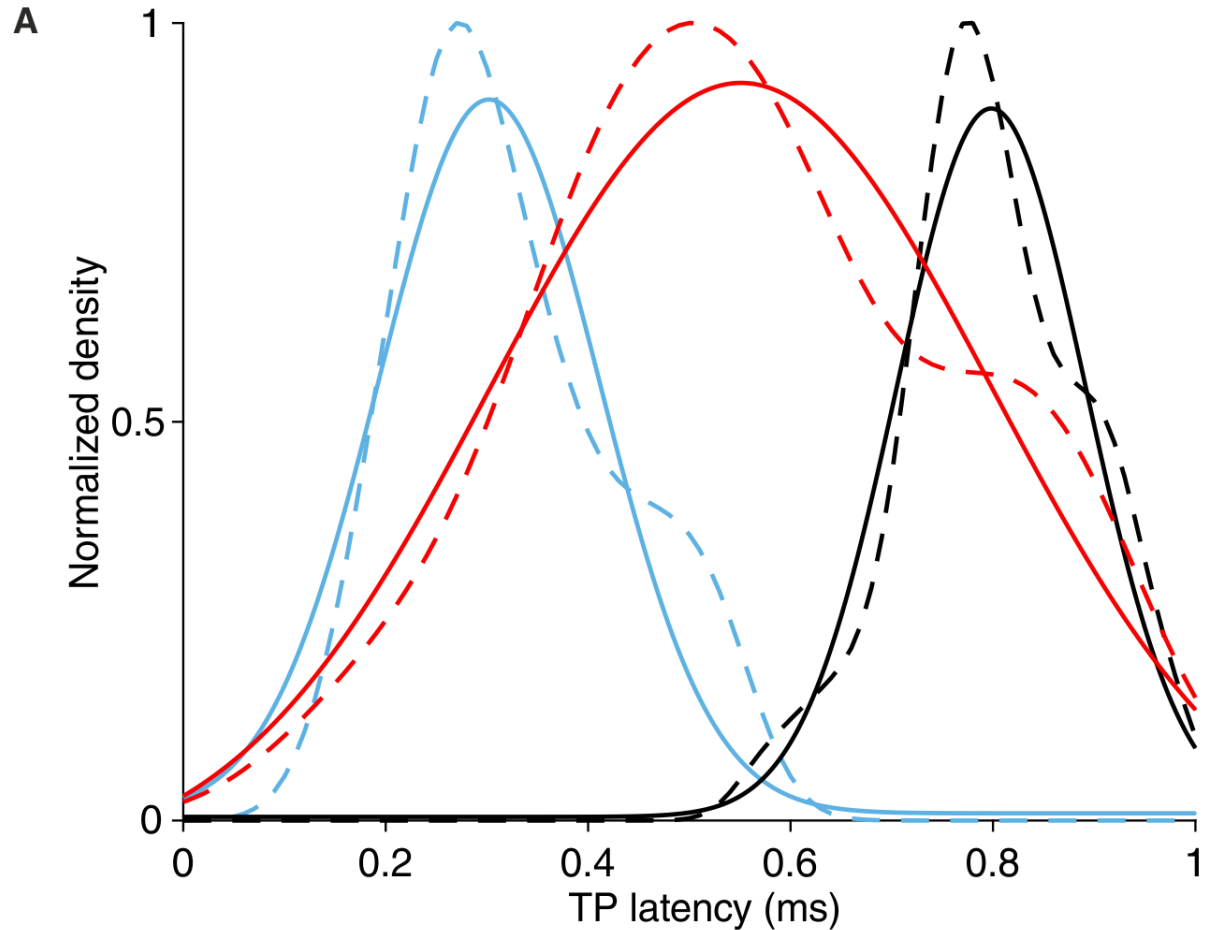
600 **(A)** Microelectrode implant location and microelectrode features. 64 channels ($n_{\text{animals}} = 15$, $n_{\text{shanks}} = 4$) and 32 channels ($n_{\text{animals}} = 3$, $n_{\text{shanks}} = 2$) microelectrodes were used in this study, analysis shown in this figure excludes data recorded with 32 channels probe due to the different spatial configuration of the channels. **(B)** Average up-state voltage deflection for each channel of the microelectrode. For experiments with drug application (either MDMA or Fen) only baseline up-states were taken in account. **(C)** Left: Average up-state voltage deflection grouped by shank. Right: Average up-state voltage deflection grouped by depths (right). Insets show the normalized correlation between averages in the two different groups. **(D)** Scatter plots showing significant correlation between shank number and peak 1 (left) and between shank number and peak 1 (right). Bold black number in each plot represent the correlation coefficient ($p < 0.001$). **(E)** Scatter plots showing significant correlation between recording channel depth and peak 1 (left) and between recording channel depth and peak 1 (right). Bold black number in each plot represent the correlation coefficient ($p < 0.001$).



613 **Figure 2-figure supplement 1. Cross-correlogram (CCG) based connectivity analysis.**
614 (A) Units are plotted according to TP latencies and repolarization time and color-coded
615 according to the number of inhibitory connections detected. Units displaying a TP latency <
616 0.55 ms were classified as putative inhibitory interneurons ('Putative int'), the remaining units
617 were classified as putative excitatory neurons ('Putative exc'). Inhibitory connections were
618 detected using Total Spiking Probability Edges (TSPE) (See Supplementary materials).
619 Putative interneurons had a 40.0 % chance of displaying at least one inhibitory connection in
620 the CCGs with an average number of 3.38 ± 0.68 inhibitory connections while putative
621 excitatory cells had a 0.33 % chance of displaying inhibitory connections. (B) Connectivity

622 scheme of one putative inhibitory unit (source unit, black circle) displaying 10 inhibitory
623 connections with surrounding clusters. Grey rhombi represent recording channels on the
624 probe with the tip of the shanks pointing north. Each colored circle represents the location of
625 an inhibited unit. Waveforms of the inhibited units are plotted nearby the location using the
626 same color. Inset shows the location of the source unit on the probe. **(C)** CCGs of the
627 connections displayed in (B) using the same color code. Solid lines represent mean, dashed
628 lines represent 1 standard deviation.

629



B

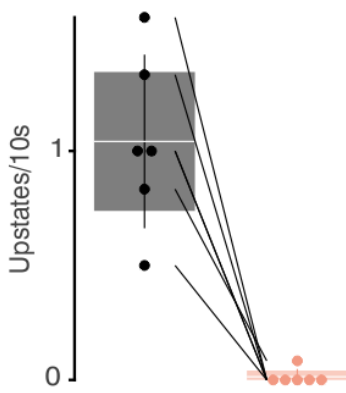
Gof metrics	Excitatory	Inhibitory	Activated
sse	0.6764	0.3036	0.5860
rsquare	0.9340	0.9669	0.9353
dfe	97	97	97
adjrsquare	0.9320	0.9659	0.9333

630 **Figure 2–figure supplement 2. TP latency density distributions.**

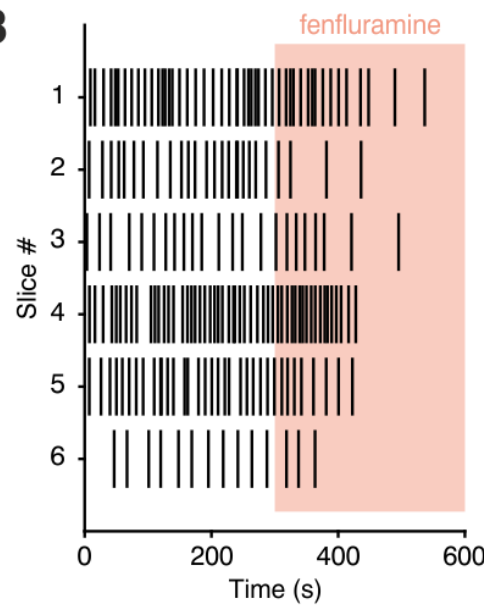
631 **(A)** Dashed lines represent kernel density estimations of probability density functions of the
632 TP latencies of putative inhibitory (blue), putative excitatory (black) and ‘activated’ units. Solid
633 lines represent gaussian fitting curves for each group. Peak inhibitory gaussian: 0.31 ms, peak
634 excitatory gaussian: 0.81 ms and peak ‘activated’ gaussian: 0.56 ms. **(B)** Goodness of fit
635 metrics for each gaussian fit. Sse = Sum of squares due to error, rsquare = R-squared
636 (coefficient of determination), dfe = Degrees of freedom in the error, adjrsquare = Degree-of-
637 freedom adjusted coefficient of determination.

638

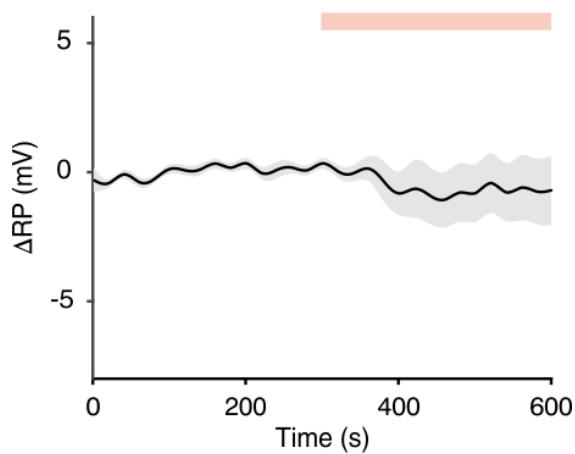
A



B

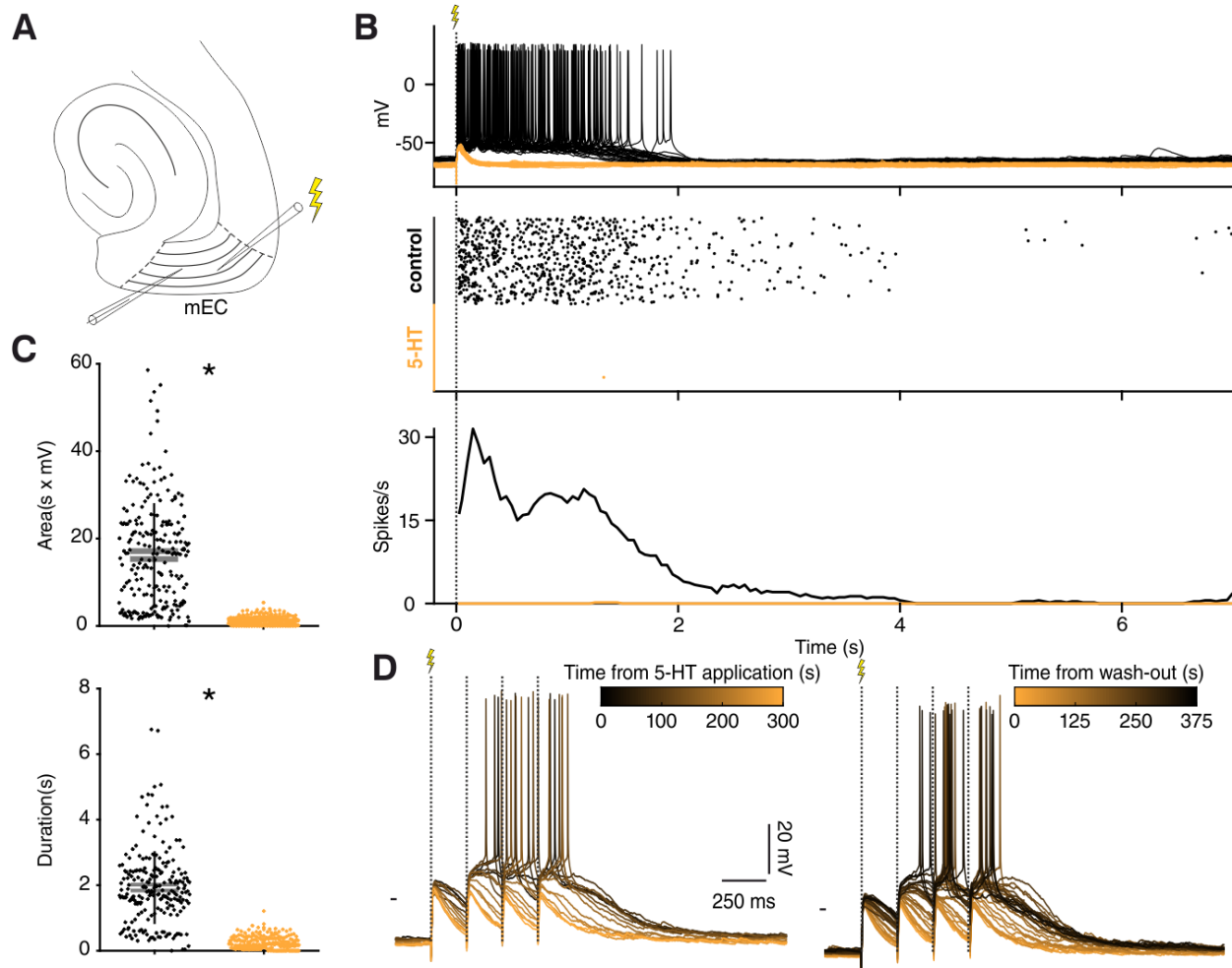


C



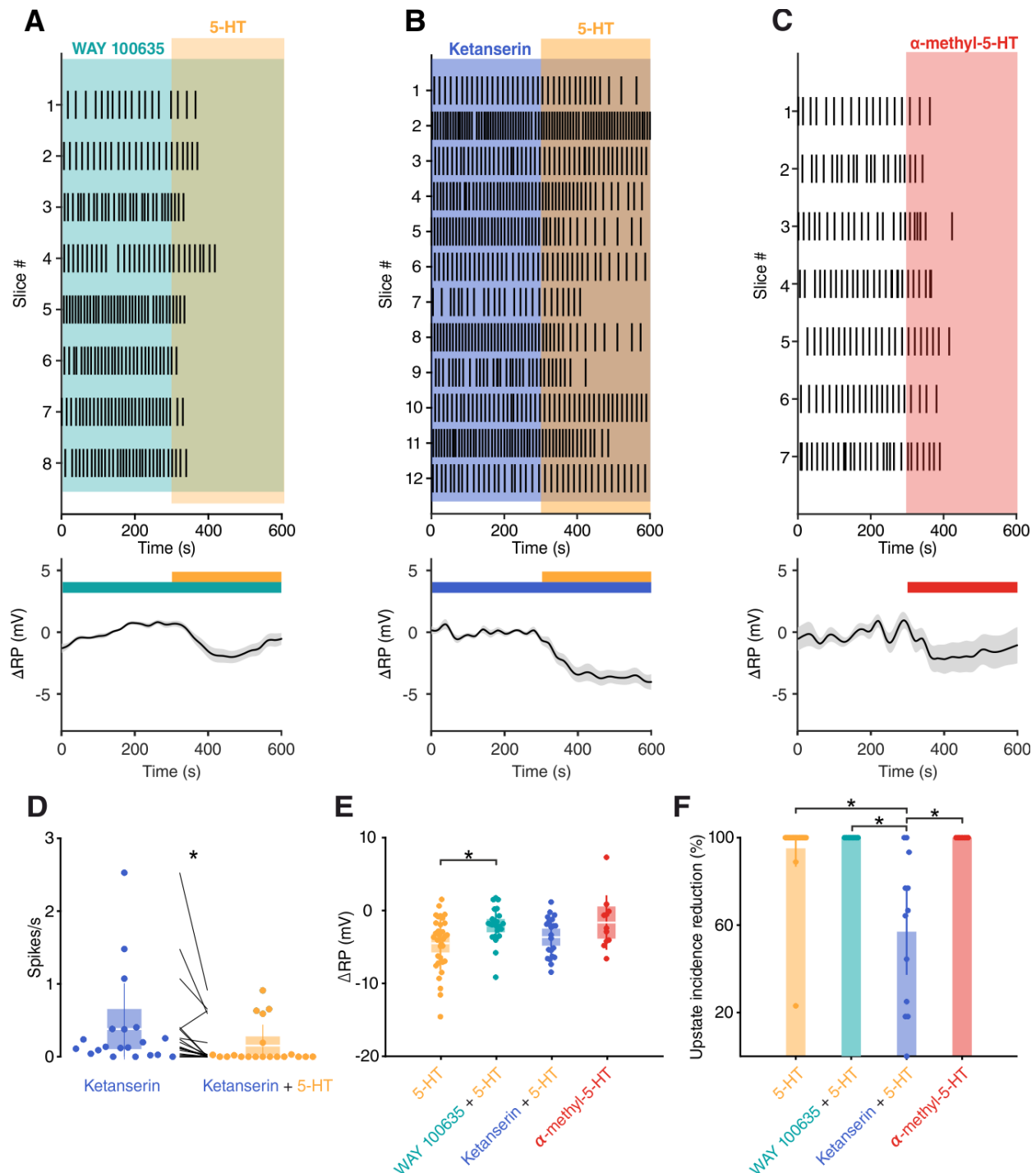
639 **Figure 3-figure supplement 1. Effect of fenfluramine on SO.**

640 **(A)** Histogram of UDS incidence before and after fenfluramine application (n= 6, baseline: 1.04
641 \pm 0.15 Up-states/10s, fenfluramine: 0.01 ± 0.01 Up-states/10s). **(B)** Up-state raster plot during
642 fenfluramine application. **(C)** Change in resting potential (RP) after fenfluramine application
643 (n=13, $\Delta RP = -0.70 \pm 1.17$ mV).



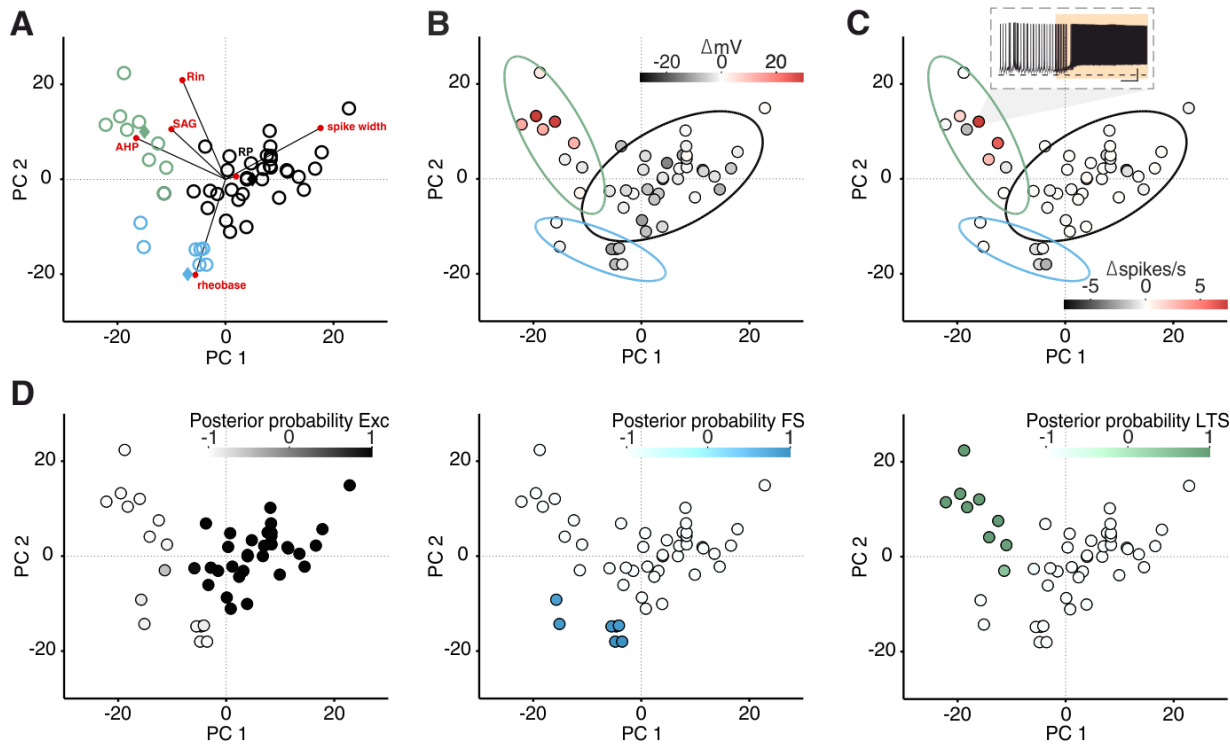
644 **Figure 3-figure supplement 2. 5-HT suppresses evoked up-states.**

645 **(A)** Experimental protocol: recording and stimulation electrode were placed in mEC layer 3,
646 stimulation electrode was located towards the lateral side of the slice. **(B)** Effect of electrical
647 stimulation before (black) and after 5-HT application (orange). 5-HT consistently suppresses
648 spiking, increasing the stimulation power up to 10 times ($n = 40/80$ in 4 neurons) had no rescue
649 effect. Top: voltage responses to electrical stimulation of a representative neuron. Middle:
650 summary spike raster plot before and after 5-HT application. Bottom: spike rate line histogram
651 **(C)** Scatter plot showing area (top, $n = 8$ neurons, $\text{mean}_{\text{control}} = 16.22 \pm 0.80$, $\text{mean}_{5\text{-HT}} = 1.24 \pm 0.97$, $p < 10^{-4}$, Wilcoxon matched-pairs signed rank test) and duration (bottom, $n = 8$ neurons, $\text{mean}_{\text{control}} = 1.92 \pm 0.07$, $\text{mean}_{5\text{-HT}} = 0.24 \pm 0.01$, $p < 10^{-4}$, Wilcoxon matched-pairs signed rank test) of evoked up-states before (black) and after 5-HT application (orange).
652 **(D)** Representative voltage responses to 1 second 4 Hz stimulation following wash-in (left) and
653 wash-out (right) of 5-HT. 5-HT prevents spiking from input summation.
654



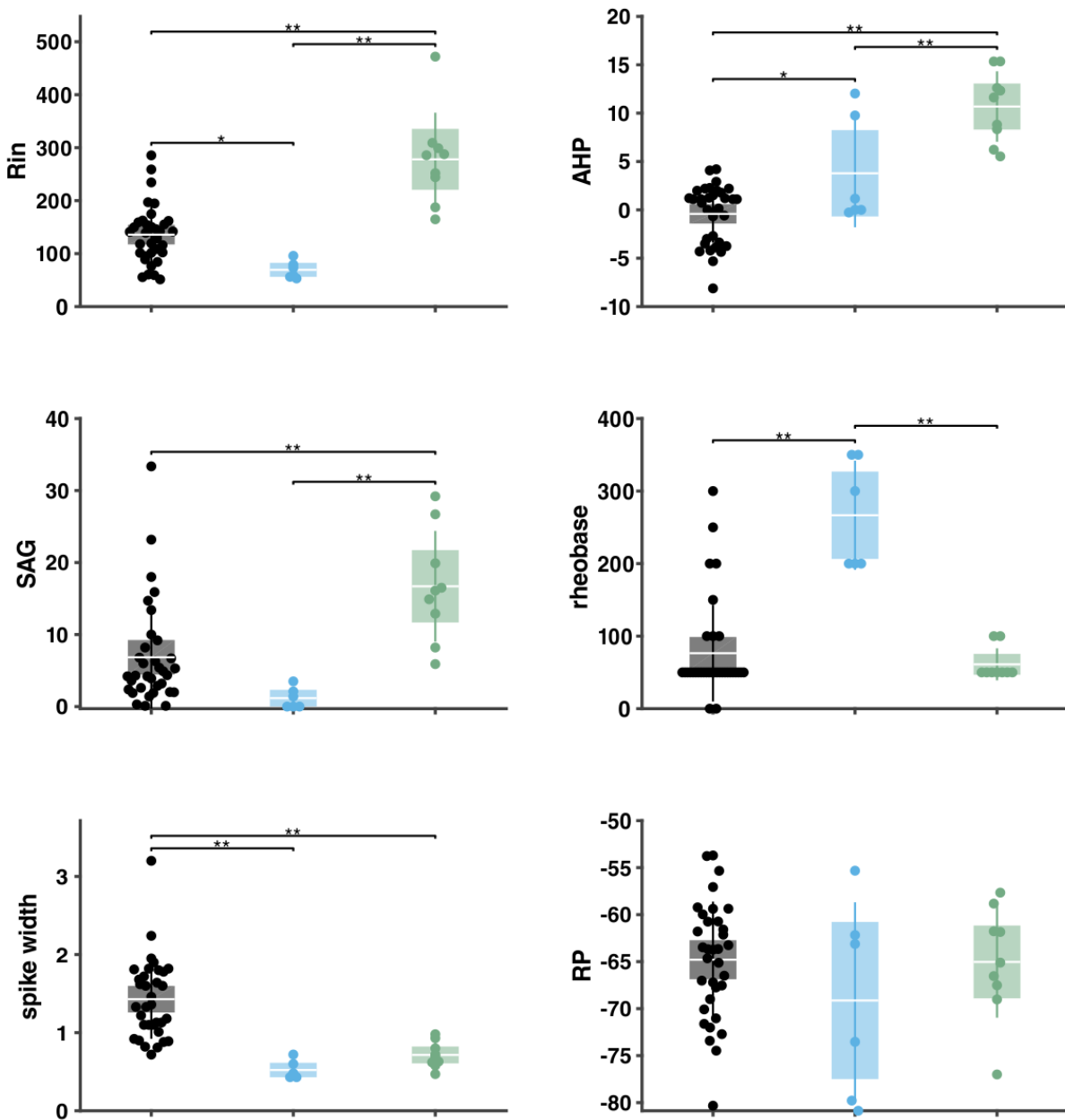
657 **Figure 3-figure supplement 3. 5-HT_{2A}Rs are involved in 5-HT mediated SO suppression.**
658 (A) Top: Up-state raster plot during application of WAY 100635 (5-HT_{1A} antagonist) + 5-HT.
659 Bottom: Change in RP in putative excitatory cells after application of WAY 100635 (5-HT_{1A}
660 antagonist) + 5-HT (n = 25 cells). (B) Top: Up-state raster plot during application of ketanserin
661 (5-HT_{2A} antagonist) + 5-HT. Bottom: Change in RP in putative excitatory cells after application
662 of ketanserin (5-HT_{2A} antagonist) + 5-HT (n = 21 cells). (C) Top: Up-state raster plot during
663 application of α-methyl-5-HT (5-HT₂ agonist). Bottom: Change in RP in putative excitatory
664 cells after application of α-methyl-5-HT (5-HT₂ agonist) (n = 11 cells). (D) Dot plot showing
665 spiking rate before and after ketanserin + 5-HT (n=20, ketanserin: 0.38 ± 0.14 spikes/s,
666 ketanserin + 5-HT: 0.15 ± 0.06 spikes/s, p= 0.011, Wilcoxon signed rank test). (E) Dot plot
667 showing change in RP for each pharmacological condition (5-HT: -4.52 ± 0.64 mV, WAY + 5-

668 HT: -2.09 ± 0.47 mV, ketanserin + 5-HT: -3.68 ± 0.60 mV and α -methyl-5-HT: -1.67 ± 1.13
669 mV; $p = 0.0329$, Kruskal-Wallis with Dunn's multiple comparisons test). **(F)** Dot plot showing
670 percentage reduction of up-states incidence for each pharmacological condition (5-HT: $95 \pm$
671 4 %, WAY + 5-HT: 100 ± 0 %, ketanserin + 5-HT: 57 ± 10.1 % and α -methyl-5-HT: 100 ± 0
672 %; $p < 10^{-4}$, Kruskal-Wallis with Dunn's multiple comparisons test).
673



674 **Figure 3-figure supplement 4. LTS neurons are depolarized by 5-HT.**
675 **(A)** PCA projection plot of all the cells recorded. Cells are color coded according to group
676 identity: excitatory (black), fast spiking (blue), low-threshold spiking (orange) and layer II
677 stellate (grey). Empty circles represent PCA loadings. **(B)** PCA projection plot color coded
678 according to ΔRP after 5-HT application. Inset shows a recording from one LTS neuron during
679 5-HT application. Scale bars: 20 mV, 25 s. Dotted line showing -70 mV. **(C)** PCA projection
680 plot color coded according to $\Delta \text{spikes/s}$ after 5-HT application. **(D)** Posterior probability of
681 being classified as Exc, FS or LTS.
682

A



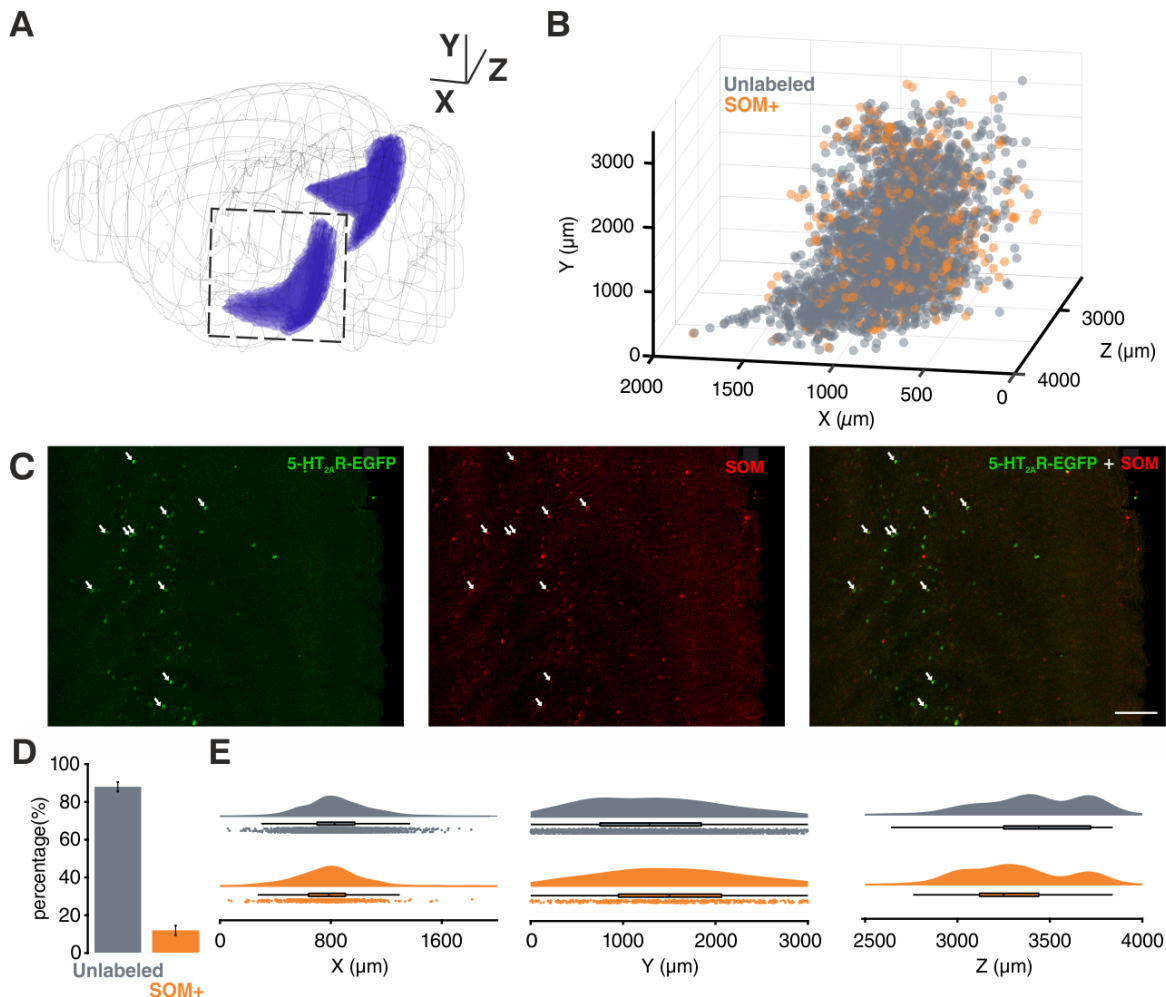
B

	Exc	FS	LTS
Rin	277.97 ± 57.52	69.38 ± 13.20	135.77 ± 18.47
AHP	10.68 ± 2.38	3.78 ± 4.46	-0.42 ± 1.00
SAG	16.70 ± 5.03	1.17 ± 1.16	6.84 ± 2.40
RP	61.11 ± 14.40	266.67 ± 60.23	76.47 ± 22.37
Rheobase	0.71 ± 0.11	0.52 ± 0.09	1.43 ± 0.17
Spike width	-65.03 ± 3.87	-69.13 ± 8.36	-64.80 ± 2.08

683 **Figure 3-figure supplement 5. Excitatory, fast-spiking and LTS cells have unique sets of**
 684 **electrophysiological features.**

685 (A) Box plot showing the values of input resistance (R_{in}), delta after-hyperpolarization (ΔAHP),
 686 SAG, RP, rheobase and spike width of excitatory (Exc, black), fast spiking (FS, blue) and low-

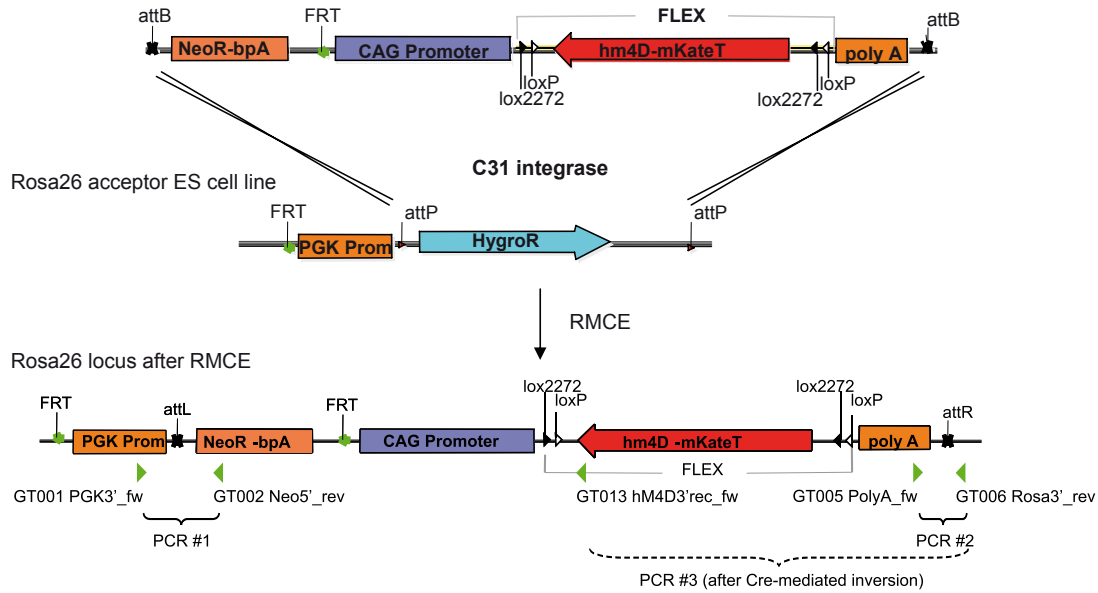
687 threshold spiking (LTS, green) cells ($n_{EXC} = 33$, $n_{FS} = 6$, $n_{LTS} = 9$; asterisk means $p < 0.05$, double
688 asterisk means $p < 0.01$). **(B)** Table showing values plotted in (A).
689



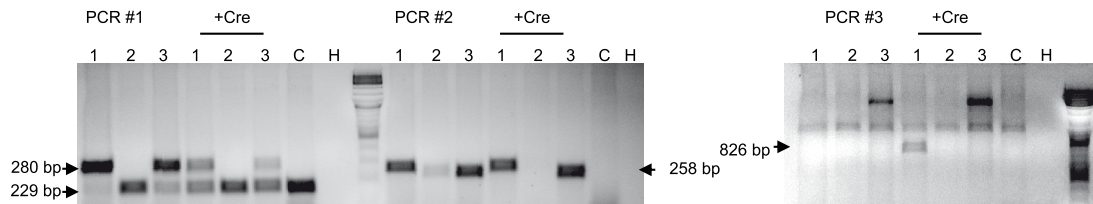
690 **Figure 3-figure supplement 6. Spatial localization of 5-HT_{2A}R positive cells in EC.**
691 **(A)** 3D visualization of EC (purple). **(B)** 3D localization of all the 5-HT_{2A}R positive cells detected
692 in EC using same perspective as (A). **(C and D)** Co-localization of 5-HT_{2A}R and Som, arrows
693 point to colocalized cells (scale bar: 100 μ m, $n_{\text{animals}}=7$, total number of 5-HT_{2A}R positive cells
694 = 3570, average number of 5-HT_{2A}R positive cells per animal = 510 ± 80.32). **(E)** Spatial
695 distribution of 5-HT_{2A}R positive cells and colocalized cells along the 3 dimensions depicted in
696 (A) (Z dimension centered on the midline).

697

A pRMCE-CAG-FLEX-hM4D-mKateT (plasmid)



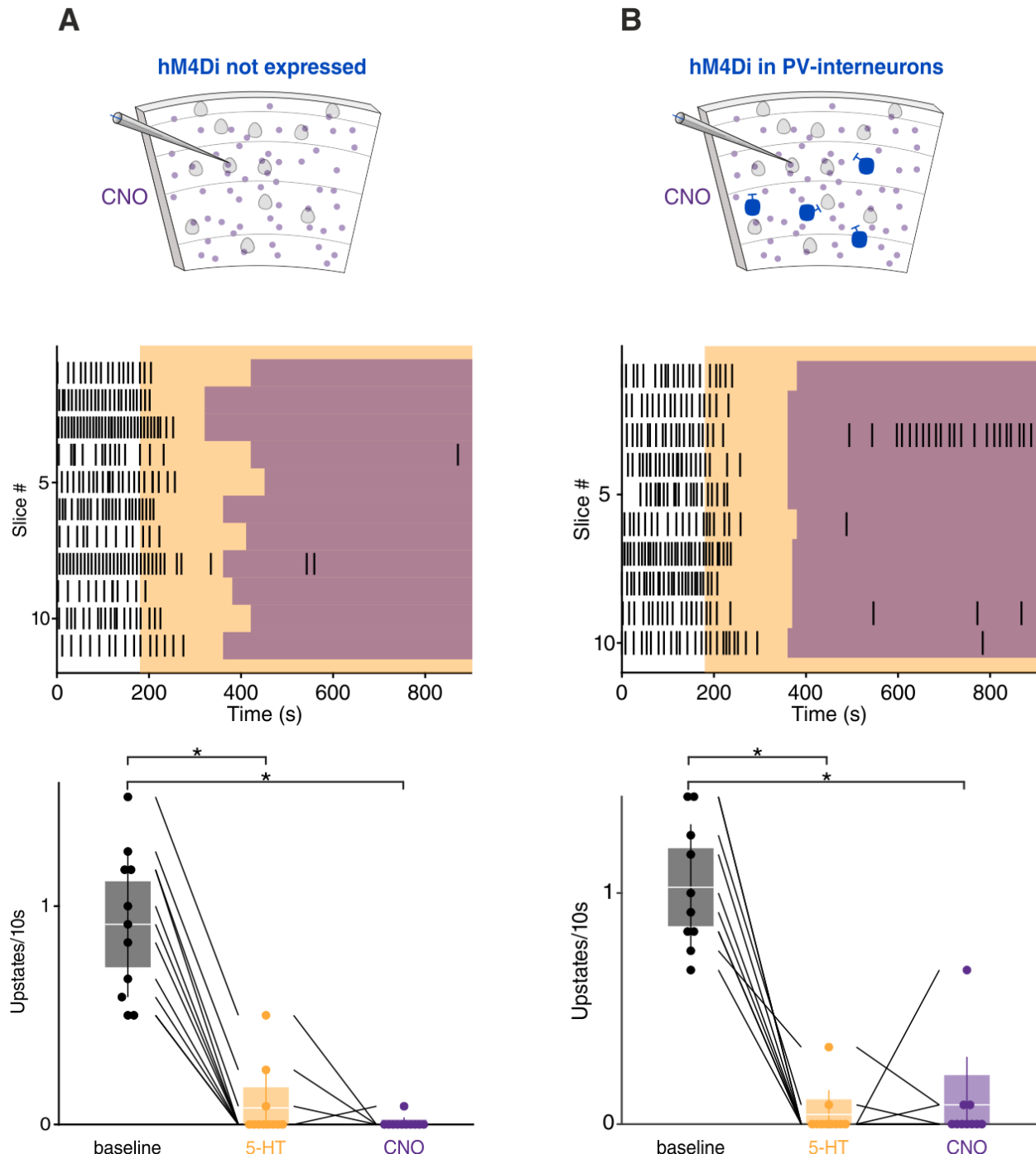
B



698 **Figure 4-figure supplement 1. Vector construction and RMCE for the generation of a**
699 **transgenic mouse line with Cre-conditional hM4Di expression.**

700 **(A)** The coding sequence of hM4Di-mKate flanked by two opposing *loxP* and *lox2272* sites
701 was placed in reverse orientation to the CAG- promoter in the pRMCE. In the acceptor ES
702 cells the ROSA26 allele harbours a PGK promoter driving the hygromycin selection marker,
703 flanked by two attP sites. RMCE by C31int replaces the hygromycin resistance by the
704 neomycin resistance of the donor vector. Location of primer binding sites in the Rosa26-
705 hM4Di locus is indicated by green triangles. **(B)** Identification of successful genomic
706 integration events and Cre-mediated inversion of the hM4Di coding sequence by PCRs. PCR
707 1 and PCR 2 test for correct integration of the 5' and 3' end of the construct into the ROSA26
708 locus. The lower band in PCR 1 results from the Neomycin resistance cassette of the feeder
709 cells in the ES cell culture. PCR 3 tests for successful recombination of the FLEX site by Cre.
710 A successful Cre-mediated recombination of the FLEX cassette was observed for clone 1,
711 resulting in an 826 bp product in PCR 3. C: control cells (not electroporated), H: H₂O input.

712



713 **Figure 5-figure supplement 1. CNO application in wildtype littermates and PV-hM4Di**
714 **mice.**

715 **(A)** CNO application in wildtype littermates. Top: Experimental protocol. Orange box
716 represents 5-HT and purple boxes represent CNO application. Bottom: Up-state incidence
717 during 5-HT and 5-HT+CNO application, patches represent 95% confidence interval, lines
718 represent standard deviation ($n = 11$ cells in 4 mice, mean _{baseline} = 0.91 ± 0.10 , mean _{5-HT} = 0.09 ± 0.04 , mean _{CNO} = 0.01 ± 0.01 , $p_{\text{baseline vs 5-HT}} = 0.0004$, $p_{\text{baseline vs CNO}} < 10^{-4}$, Kruskal-Wallis test)
719 **(B)** Same as (A) but in PV-hM4Di mice ($n = 10$ cells in 4 mice, mean _{baseline} = 1.02 ± 0.08 ,
720 mean _{5-HT} = 0.04 ± 0.03 , mean _{CNO} = 0.08 ± 0.07 , $p_{\text{baseline vs 5-HT}} < 10^{-4}$, $p_{\text{baseline vs CNO}} = 0.0003$,
721 Kruskal-Wallis test).

723 References

724 ABI-SAAB, W. M., BUBSER, M., ROTH, R. H. & DEUTCH, A. Y. 1999. 5-HT2 receptor
725 regulation of extracellular GABA levels in the prefrontal cortex.
726 *Neuropsychopharmacology*, 20, 92-6.

727 ANTOINE, M. W., LANGBERG, T., SCHNEPEL, P. & FELDMAN, D. E. 2019. Increased
728 Excitation-Inhibition Ratio Stabilizes Synapse and Circuit Excitability in Four Autism
729 Mouse Models. *Neuron*, 101, 648-661.e4.

730 ARMBRUSTER, B. N., LI, X., PAUSCH, M. H., HERLITZE, S. & ROTH, B. L. 2007. Evolving
731 the lock to fit the key to create a family of G protein-coupled receptors potently
732 activated by an inert ligand. *Proc Natl Acad Sci U S A*, 104, 5163-8.

733 ASHBY, C. R., JR., JIANG, L. H., KASSER, R. J. & WANG, R. Y. 1990. Electrophysiological
734 characterization of 5-hydroxytryptamine2 receptors in the rat medial prefrontal
735 cortex. *J Pharmacol Exp Ther*, 252, 171-8.

736 ATHILINGAM, J. C., BEN-SHALOM, R., KEESHEN, C. M., SOHAL, V. S. & BENDER, K. J.
737 2017. Serotonin enhances excitability and gamma frequency temporal integration in
738 mouse prefrontal fast-spiking interneurons. *eLife*, 6, e31991.

739 AZIMI, Z., BARZAN, R., SPOIDA, K., SURDIN, T., WOLLENWEBER, P., MARK, M. D.,
740 HERLITZE, S. & JANCKE, D. 2020. Separable gain control of ongoing and evoked
741 activity in the visual cortex by serotonergic input. *eLife*, 9, e53552.

742 BARTHÓ, P., HIRASE, H., MONCONDUIT, L., ZUGARO, M., HARRIS, K. D. & BUZSÁKI, G.
743 2004. Characterization of neocortical principal cells and interneurons by network
744 interactions and extracellular features. *J Neurophysiol*, 92, 600-8.

745 CARHART-HARRIS, R. L. & FRISTON, K. J. 2019. REBUS and the Anarchic Brain: Toward a
746 Unified Model of the Brain Action of Psychedelics. *Pharmacol Rev*, 71, 316-344.

747 CARHART-HARRIS, R. L., MUTHUKUMARASWAMY, S., ROSEMAN, L., KAELEN, M.,
748 DROOG, W., MURPHY, K., TAGLIAZUCCHI, E., SCHENBERG, E. E., NEST, T.,
749 ORBAN, C., LEECH, R., WILLIAMS, L. T., WILLIAMS, T. M., BOLSTRIDGE, M.,
750 SESSA, B., MCGONIGLE, J., SERENO, M. I., NICHOLS, D., HELLYER, P. J.,
751 HOBDEN, P., EVANS, J., SINGH, K. D., WISE, R. G., CURRAN, H. V., FEILDING, A. &
752 NUTT, D. J. 2016. Neural correlates of the LSD experience revealed by multimodal
753 neuroimaging. *Proc Natl Acad Sci U S A*, 113, 4853-8.

754 CHALMERS, D. T. & WATSON, S. J. 1991. Comparative anatomical distribution of 5-HT1A
755 receptor mRNA and 5-HT1A binding in rat brain--a combined in situ hybridisation/in
756 vitro receptor autoradiographic study. *Brain Res*, 561, 51-60.

757 CHEN, N., SUGIHARA, H. & SUR, M. 2015. An acetylcholine-activated microcircuit drives
758 temporal dynamics of cortical activity. *Nat Neurosci*, 18, 892-902.

759 DE BLASI, S., CIBA, M., BAHMER, A. & THIELEMANN, C. 2019. Total spiking probability
760 edges: A cross-correlation based method for effective connectivity estimation of
761 cortical spiking neurons. *J Neurosci Methods*, 312, 169-181.

762 DESCARRIES, L., RIAD, M. & PARENT, M. 2010. CHAPTER 1.4 - Ultrastructure of the
763 Serotonin Innervation in the Mammalian Central Nervous System. In: MÜLLER, C. P.
764 & JACOBS, B. L. (eds.) *Handbook of Behavioral Neuroscience*. Elsevier.

765 FANSELOW, E. E., RICHARDSON, K. A. & CONNORS, B. W. 2008. Selective, state-
766 dependent activation of somatostatin-expressing inhibitory interneurons in mouse
767 neocortex. *J Neurophysiol*, 100, 2640-52.

768 FREI, E., GAMMA, A., PASCUAL-MARQUI, R., LEHMANN, D., HELL, D. & VOLLENWEIDER,
769 F. X. 2001. Localization of MDMA-induced brain activity in healthy volunteers using
770 low resolution brain electromagnetic tomography (LORETA). *Hum Brain Mapp*, 14,
771 152-65.

772 FUNK, C. M., PEELMAN, K., BELLESI, M., MARSHALL, W., CIRELLI, C. & TONONI, G.
773 2017. Role of Somatostatin-Positive Cortical Interneurons in the Generation of Sleep
774 Slow Waves. *J Neurosci*, 37, 9132-9148.

775 GIBSON, J. R., BEIERLEIN, M. & CONNORS, B. W. 1999. Two networks of electrically
776 coupled inhibitory neurons in neocortex. *Nature*, 402, 75-9.

777 GRANDJEAN, J., CORCOBA, A., KAHN, M. C., UPTON, A. L., DENERIS, E. S., SEIFRITZ, E.,
778 HELMCHEN, F., MANN, E. O., RUDIN, M. & SAAB, B. J. 2019. A brain-wide
779 functional map of the serotonergic responses to acute stress and fluoxetine. *Nat
780 Commun*, 10, 350.

781 GREEN, A. R., MECHAN, A. O., ELLIOTT, J. M., O'SHEA, E. & COLADO, M. I. 2003. The
782 Pharmacology and Clinical Pharmacology of 3,4-Methylenedioxymethamphetamine
783 (MDMA, "Ecstasy"). *Pharmacological Reviews*, 55, 463-508.

784 HARDEBO, J. E. & OWMAN, C. 1980. Barrier mechanisms for neurotransmitter monoamines
785 and their precursors at the blood-brain interface. *Ann Neurol*, 8, 1-31.

786 HARDY, A., PALOUZIER-PAULIGNAN, B., DUCHAMP, A., ROYET, J. P. & DUCHAMP-
787 VIRET, P. 2005. 5-Hydroxytryptamine action in the rat olfactory bulb: in vitro
788 electrophysiological patch-clamp recordings of juxtaglomerular and mitral cells.
789 *Neuroscience*, 131, 717-31.

790 HARRIS, K. D. & THIELE, A. 2011. Cortical state and attention. *Nat Rev Neurosci*, 12, 509-
791 23.

792 HAYES, D. J. & GREENSHAW, A. J. 2011. 5-HT receptors and reward-related behaviour: a
793 review. *Neurosci Biobehav Rev*, 35, 1419-49.

794 HITZ, C., STEUBER-BUCHBERGER, P., DELIC, S., WURST, W. & KUHN, R. 2009.
795 Generation of shRNA transgenic mice. *Methods Mol Biol*, 530, 101-29.

796 HITZ, C., WURST, W. & KUHN, R. 2007. Conditional brain-specific knockdown of MAPK
797 using Cre/loxP regulated RNA interference. *Nucleic Acids Res*, 35, e90.

798 KAUR, S., JUNEK, A., BLACK, M. A. & SEMBA, K. 2008. Effects of ibotenate and 192IgG-
799 saporin lesions of the nucleus basalis magnocellularis/substantia innominata on
800 spontaneous sleep and wake states and on recovery sleep after sleep deprivation in
801 rats. *J Neurosci*, 28, 491-504.

802 KOMETER, M., POKORNY, T., SEIFRITZ, E. & VOLLEINWEIDER, F. X. 2015. Psilocybin-
803 induced spiritual experiences and insightfulness are associated with synchronization
804 of neuronal oscillations. *Psychopharmacology (Berl)*, 232, 3663-76.

805 KUYPERS, K. P. C., DE LA TORRE, R., FARRE, M., PIZARRO, N., XICOTA, L. &
806 RAMAEKERS, J. G. 2018. MDMA-induced indifference to negative sounds is
807 mediated by the 5-HT2A receptor. *Psychopharmacology (Berl)*, 235, 481-490.

808 KVITSIANI, D., RANADE, S., HANGYA, B., TANIGUCHI, H., HUANG, J. Z. & KEPECS, A.
809 2013. Distinct behavioural and network correlates of two interneuron types in
810 prefrontal cortex. *Nature*, 498, 363-6.

811 LANSBERGEN, M. M., DUMONT, G. J. H., VAN GERVEN, J. M. A., BUITELAAR, J. K. &
812 VERKES, R.-J. 2011. Acute effects of MDMA (3,4-methylenedioxymethamphetamine)
813 on EEG oscillations: alone and in combination with ethanol or THC (delta-9-
814 tetrahydrocannabinol). *Psychopharmacology*, 213, 745-756.

815 LEE, S. H. & DAN, Y. 2012. Neuromodulation of brain states. *Neuron*, 76, 209-22.

816 LIECHTI, M. E., SAUR, M. R., GAMMA, A., HELL, D. & VOLLENWEIDER, F. X. 2000.
817 Psychological and Physiological Effects of MDMA ("Ecstasy") after Pretreatment with
818 the 5-HT2 Antagonist Ketanserin in Healthy Humans. *Neuropsychopharmacology*, 23,
819 396-404.

820 LIN, L. C. & SIBILLE, E. 2015. Somatostatin, neuronal vulnerability and behavioral
821 emotionality. *Mol Psychiatry*, 20, 377-87.

822 LOTTEM, E., LÖRINCZ, M. L. & MAINEN, Z. F. 2016. Optogenetic Activation of Dorsal
823 Raphe Serotonin Neurons Rapidly Inhibits Spontaneous But Not Odor-Evoked
824 Activity in Olfactory Cortex. *J Neurosci*, 36, 7-18.

825 MAREK, G. J. & AGHAJANIAN, G. K. 1994. Excitation of interneurons in piriform cortex by
826 5-hydroxytryptamine: blockade by MDL 100,907, a highly selective 5-HT2A receptor
827 antagonist. *Eur J Pharmacol*, 259, 137-41.

828 MAREK, G. J., CARPENTER, L. L., MCDOUGLE, C. J. & PRICE, L. H. 2003. Synergistic
829 action of 5-HT2A antagonists and selective serotonin reuptake inhibitors in
830 neuropsychiatric disorders. *Neuropsychopharmacology*, 28, 402-12.

831 MARTIN, D. A. & NICHOLS, C. D. 2016. Psychedelics Recruit Multiple Cellular Types and
832 Produce Complex Transcriptional Responses Within the Brain. *EBioMedicine*, 11,
833 262-277.

834 MCGINTY, D. J. & HARPER, R. M. 1976. Dorsal raphe neurons: depression of firing during
835 sleep in cats. *Brain Research*, 101, 569-575.

836 MELTZER, H. Y. 1999. The role of serotonin in antipsychotic drug action.
837 *Neuropsychopharmacology*, 21, 106s-115s.

838 MICHAIEL, A. M., PARKER, P. R. L. & NIELL, C. M. 2019. A Hallucinogenic Serotonin-2A
839 Receptor Agonist Reduces Visual Response Gain and Alters Temporal Dynamics in
840 Mouse V1. *Cell Rep*, 26, 3475-3483.e4.

841 MONTI, J. M. 2011. Serotonin control of sleep-wake behavior. *Sleep Med Rev*, 15, 269-81.

842 MURAYAMA, M., PÉREZ-GARCI, E., NEVIAN, T., BOCK, T., SENN, W. & LARKUM, M. E.
843 2009. Dendritic encoding of sensory stimuli controlled by deep cortical interneurons.
844 *Nature*, 457, 1137-1141.

845 MUTHUKUMARASWAMY, S. D., CARHART-HARRIS, R. L., MORAN, R. J., BROOKES, M.
846 J., WILLIAMS, T. M., ERRTIZOE, D., SESSA, B., PAPADOPOULOS, A.,
847 BOLSTRIDGE, M., SINGH, K. D., FEILDING, A., FRISTON, K. J. & NUTT, D. J. 2013.
848 Broadband cortical desynchronization underlies the human psychedelic state. *J
849 Neurosci*, 33, 15171-83.

850 MUZERELLE, A., SCOTTO-LOMASSESE, S., BERNARD, J. F., SOIZA-REILLY, M. &
851 GASPAR, P. 2016. Conditional anterograde tracing reveals distinct targeting of
852 individual serotonin cell groups (B5-B9) to the forebrain and brainstem. *Brain
853 Structure and Function*, 221, 535-561.

854 NAKAI, N., NAGANO, M., SAITOW, F., WATANABE, Y., KAWAMURA, Y., KAWAMOTO, A.,
855 TAMADA, K., MIZUMA, H., ONOE, H., WATANABE, Y., MONAI, H., HIRASE, H.,
856 NAKATANI, J., INAGAKI, H., KAWADA, T., MIYAZAKI, T., WATANABE, M., SATO, Y.,
857 OKABE, S., KITAMURA, K., KANO, M., HASHIMOTO, K., SUZUKI, H. & TAKUMI, T.
858 2017. Serotonin rebalances cortical tuning and behavior linked to autism symptoms
859 in 15q11-13 CNV mice. *Sci Adv*, 3, e1603001.

860 NESKE, G. T. 2015. The Slow Oscillation in Cortical and Thalamic Networks: Mechanisms
861 and Functions. *Front Neural Circuits*, 9, 88.

862 NESKE, G. T., PATRICK, S. L. & CONNORS, B. W. 2015. Contributions of diverse excitatory
863 and inhibitory neurons to recurrent network activity in cerebral cortex. *J Neurosci*, 35,
864 1089-105.

865 NICHOLS, D. E. 2016. Psychedelics. *Pharmacol Rev*, 68, 264-355.

866 NICHOLS, D. E. & NICHOLS, C. D. 2008. Serotonin Receptors. *Chemical Reviews*, 108,
867 1614-1641.

868 NIETHARD, N., NGO, H. V., EHRLICH, I. & BORN, J. 2018. Cortical circuit activity underlying
869 sleep slow oscillations and spindles. *Proc Natl Acad Sci U S A*, 115, E9220-e9229.

870 OBERMAYER, J., HEISTEK, T. S., KERKHOFS, A., GORIOUNOVA, N. A., KROON, T.,
871 BAAYEN, J. C., IDEMA, S., TESTA-SILVA, G., COUEY, J. J. & MANSVELDER, H. D.
872 2018. Lateral inhibition by Martinotti interneurons is facilitated by cholinergic inputs in
873 human and mouse neocortex. *Nat Commun*, 9, 4101.

874 OIKONOMOU, G., ALTERMATT, M., ZHANG, R. W., COUGHLIN, G. M., MONTZ, C.,
875 GRADINARU, V. & PROBER, D. A. 2019. The Serotonergic Raphe Promote Sleep in
876 Zebrafish and Mice. *Neuron*, 103, 686-701.e8.

877 PANTAZOPOULOS, H., WISEMAN, J. T., MARKOTA, M., EHRENFIELD, L. & BERRETTA, S.
878 2017. Decreased Numbers of Somatostatin-Expressing Neurons in the Amygdala of
879 Subjects With Bipolar Disorder or Schizophrenia: Relationship to Circadian Rhythms.
880 *Biol Psychiatry*, 81, 536-547.

881 PETZOLD, G. C., HAGIWARA, A. & MURTHY, V. N. 2009. Serotonergic modulation of odor
882 input to the mammalian olfactory bulb. *Nature Neuroscience*, 12, 784-791.

883 PRELLER, K. H., BURT, J. B., JI, J. L., SCHLEIFER, C. H., ADKINSON, B. D., STAMPFLI, P.,
884 SEIFRITZ, E., REPOVS, G., KRYSTAL, J. H., MURRAY, J. D., VOLLENWEIDER, F. X.
885 & ANTICEVIC, A. 2018. Changes in global and thalamic brain connectivity in LSD-
886 induced altered states of consciousness are attributable to the 5-HT2A receptor.
887 *Elife*, 7.

888 PUIG, M. V., WATAKABE, A., USHIMARU, M., YAMAMORI, T. & KAWAGUCHI, Y. 2010.
889 Serotonin modulates fast-spiking interneuron and synchronous activity in the rat
890 prefrontal cortex through 5-HT1A and 5-HT2A receptors. *J Neurosci*, 30, 2211-22.

891 RANGANATHAN, G. N., APOSTOLIDES, P. F., HARNETT, M. T., XU, N. L., DRUCKMANN,
892 S. & MAGEE, J. C. 2018. Active dendritic integration and mixed neocortical network
893 representations during an adaptive sensing behavior. *Nat Neurosci*, 21, 1583-1590.

894 RENART, A., DE LA ROCHA, J., BARTHO, P., HOLLENDER, L., PARGA, N., REYES, A. &
895 HARRIS, K. D. 2010. The asynchronous state in cortical circuits. *Science*, 327, 587-
896 90.

897 ROTHMAN, R. B. & BAUMANN, M. H. 2002. Therapeutic and adverse actions of serotonin
898 transporter substrates. *Pharmacol Ther*, 95, 73-88.

899 ROUX, L., STARK, E., SJULSON, L. & BUZSAKI, G. 2014. In vivo optogenetic identification
900 and manipulation of GABAergic interneuron subtypes. *Curr Opin Neurobiol*, 26, 88-
901 95.

902 SANCHEZ-VIVES, M. V., MASSIMINI, M. & MATTIA, M. 2017. Shaping the Default Activity
903 Pattern of the Cortical Network. *Neuron*, 94, 993-1001.

904 SCHMITZ, D., GLOVELI, T., EMPSON, R. M., DRAGUHN, A. & HEINEMANN, U. 1998.
905 Serotonin reduces synaptic excitation in the superficial medial entorhinal cortex of the
906 rat via a presynaptic mechanism. *J Physiol*, 508 (Pt 1), 119-29.

907 SCHNUTGEN, F., DOERFLINGER, N., CALLEJA, C., WENDLING, O., CHAMBON, P. &
908 GHYSELINCK, N. B. 2003. A directional strategy for monitoring Cre-mediated
909 recombination at the cellular level in the mouse. *Nat Biotechnol*, 21, 562-5.

910 SEILLIER, L., LORENZ, C., KAWAGUCHI, K., OTT, T., NIEDER, A., POURRIAHI, P. &
911 NIENBORG, H. 2017. Serotonin Decreases the Gain of Visual Responses in Awake
912 Macaque V1. *J Neurosci*, 37, 11390-11405.

913 SENZAI, Y., FERNANDEZ-RUIZ, A. & BUZSAKI, G. 2019. Layer-Specific Physiological
914 Features and Interlaminar Interactions in the Primary Visual Cortex of the Mouse.
915 *Neuron*, 101, 500-513 e5.

916 SHAMASH, P., CARANDINI, M., HARRIS, K. & STEINMETZ, N. 2018. A tool for analyzing
917 electrode tracks from slice histology. *bioRxiv*, 447995.

918 SHELDON, P. W. & AGHAJANIAN, G. K. 1990. Serotonin (5-HT) induces IPSPs in pyramidal
919 layer cells of rat piriform cortex: evidence for the involvement of a 5-HT2-activated
920 interneuron. *Brain Res*, 506, 62-9.

921 SIPPY, T. & YUSTE, R. 2013. Decorrelating action of inhibition in neocortical networks. *J
922 Neurosci*, 33, 9813-30.

923 SMITH, S. L., SMITH, I. T., BRANCO, T. & HÄUSSER, M. 2013. Dendritic spikes enhance
924 stimulus selectivity in cortical neurons in vivo. *Nature*, 503, 115-120.

925 STERIADE, M., NUNEZ, A. & AMZICA, F. 1993. A novel slow (< 1 Hz) oscillation of
926 neocortical neurons in vivo: depolarizing and hyperpolarizing components. *J
927 Neurosci*, 13, 3252-65.

928 STRINGER, C., PACHITARIU, M., STEINMETZ, N. A., OKUN, M., BARTHO, P., HARRIS, K.
929 D., SAHANI, M. & LESICA, N. A. 2016. Inhibitory control of correlated intrinsic
930 variability in cortical networks. *Elife*, 5.

931 STURGILL, J. F. & ISAACSON, J. S. 2015. Somatostatin cells regulate sensory response
932 fidelity via subtractive inhibition in olfactory cortex. *Nat Neurosci*, 18, 531-5.

933 TAHVILDARI, B., WOLFEL, M., DUQUE, A. & MCCORMICK, D. A. 2012. Selective functional
934 interactions between excitatory and inhibitory cortical neurons and differential
935 contribution to persistent activity of the slow oscillation. *J Neurosci*, 32, 12165-79.

936 TAKAHASHI, N., OERTNER, T. G., HEGEMANN, P. & LARKUM, M. E. 2016. Active cortical
937 dendrites modulate perception. *Science*, 354, 1587-1590.

938 TANG, Z.-Q. & TRUSSELL, L. O. 2017. Serotonergic Modulation of Sensory Representation
939 in a Central Multisensory Circuit Is Pathway Specific. *Cell reports*, 20, 1844-1854.

940 TANIGUCHI, H., HE, M., WU, P., KIM, S., PAIK, R., SUGINO, K., KVITSIANI, D., FU, Y., LU,
941 J., LIN, Y., MIYOSHI, G., SHIMA, Y., FISHELL, G., NELSON, S. B. & HUANG, Z. J.
942 2011. A resource of Cre driver lines for genetic targeting of GABAergic neurons in
943 cerebral cortex. *Neuron*, 71, 995-1013.

944 TEIXEIRA, C. M., ROSEN, Z. B., SURI, D., SUN, Q., HERSH, M., SARGIN, D., DINCHEVA, I.,
945 MORGAN, A. A., SPIVACK, S., KROK, A. C., HIRSCHFELD-STOLER, T., LAMBE, E.
946 K., SIEGELBAUM, S. A. & ANSORGE, M. S. 2018. Hippocampal 5-HT Input
947 Regulates Memory Formation and Schaffer Collateral Excitation. *Neuron*, 98, 992-
948 1004.e4.

949 TRAINITO, C., VON NICOLAI, C., MILLER, E. K. & SIEGEL, M. 2019. Extracellular Spike
950 Waveform Dissociates Four Functionally Distinct Cell Classes in Primate Cortex. *Curr
951 Biol*.

952 TREMBLAY, R., LEE, S. & RUDY, B. 2016. GABAergic Interneurons in the Neocortex: From
953 Cellular Properties to Circuits. *Neuron*, 91, 260-92.

954 TURRIGIANO, G. 2011. Too many cooks? Intrinsic and synaptic homeostatic mechanisms in
955 cortical circuit refinement. *Annu Rev Neurosci*, 34, 89-103.

956 UNDERWOOD, M. D., KASSIR, S. A., BAKALIAN, M. J., GALFALVY, H., DWORK, A. J.,
957 MANN, J. J. & ARANGO, V. 2018. Serotonin receptors and suicide, major depression,
958 alcohol use disorder and reported early life adversity. *Translational Psychiatry*, 8, 279.

959 UPHOUSE, L. & GUPTARAK, J. 2010. Serotonin and sexual behavior. *Handbook of the*
960 *behavioral neurobiology of serotonin*. San Diego, CA, US: Elsevier Academic Press.

961 URBAN-CIECKO, J., FANSELOW, E. E. & BARTH, A. L. 2015. Neocortical somatostatin
962 neurons reversibly silence excitatory transmission via GABA_A receptors. *Curr Biol*, 25,
963 722-31.

964 VAN STRIEN, N. M., CAPPAERT, N. L. & WITTER, M. P. 2009. The anatomy of memory: an
965 interactive overview of the parahippocampal-hippocampal network. *Nat Rev*
966 *Neurosci*, 10, 272-82.

967 VANDERWOLF, C. H. & BAKER, G. B. 1986. Evidence that serotonin mediates non-
968 cholinergic neocortical low voltage fast activity, non-cholinergic hippocampal
969 rhythmical slow activity and contributes to intelligent behavior. *Brain Res*, 374, 342-
970 56.

971 WILSON, N. R., RUNYAN, C. A., WANG, F. L. & SUR, M. 2012. Division and subtraction by
972 distinct cortical inhibitory networks in vivo. *Nature*, 488, 343-348.

973 WOOD, J., KIM, Y. & MOGHADDAM, B. 2012. Disruption of prefrontal cortex large scale
974 neuronal activity by different classes of psychotomimetic drugs. *J Neurosci*, 32,
975 3022-31.

976 WYSKIEL, D. R. & ANDRADE, R. 2016. Serotonin excites hippocampal CA1 GABAergic
977 interneurons at the stratum radiatum-stratum lacunosum moleculare border.
978 *Hippocampus*, 26, 1107-14.

979 ZHOU, F.-M. & HABLITZ, J. J. 1999. Activation of Serotonin Receptors Modulates Synaptic
980 Transmission in Rat Cerebral Cortex. *Journal of Neurophysiology*, 82, 2989-2999.

981